TOPICS IN HIGH VOLTAGE PULSED POWER PLASMA DEVICES AND APPLICATIONS

by

Hao Chen

A Dissertation Presented to the
FACULTY OF THE USC GRADUATE SCHOOL
UNIVERSITY OF SOUTHERN CALIFORNIA
In Partial Fulfillment of the
Requirements for the Degree
DOCTOR OF PHILOSOPHY
(ELECTRICAL ENGINEERING)

May 2010

Copyright 2010 Hao Chen

Dedication

To my parents and husband

Acknowledgments

The receptions before the talks of celebrated scientists make great reunions for graduate students. It is always interesting to have small talks about the latest research topics with these students, who are originally from all over the world, and now buried in all kinds of research explorations at USC. This is a glimpse of one of the moments that made the daily life of a student pursuing a Doctor of Philosophy a rather wonderful experience. I am one of them, enjoying the “good graduate school time” which typically starts around 10 am and goes until late at night every day.

The first person to be acknowledged in my PhD career, if I can say “career”, of course is my advisor, Professor Martin Gundersen, who maintained a rather joyful atmosphere in our research group and inspired us to produce great results with “Gundersen’s wisdom,” i.e. our group meetings! I will never forget my embarrassing moments in which I replied countless “I don’t know’s” during the group meeting presentations for the first two years of my graduate schooling. This really urged me to understand and think through every single detail in the research and motivated me to broaden my vision into multi-disciplinary knowledge, and to always look further

and deeper. I really appreciated the huge benefit later when I did the conference presentations, as well as when I explored the possibilities for the next steps in my life. Thank you Dr. Gundersen. For all the advice, all the support, and all the encouragement you have given me.

I wish to thank Dr. Thomas Vernier and Dr. Andra Kuthi. They served as my role models for how to be a serious and brilliant engineer. This has really helped me make a good transition from a pure physics student to a “physineer”.

I also would like to thank my professors and the members of my qualifying exam and defense committees, Martin Gundersen, Thomas C. Katsouleas, Patric Muggli, Robert Hellwarth, and Stephan Haas. They all transferred some part of their wisdom to me one way or another through homework problems, suggestions and constructive criticism.

It has been my pleasure and a wonderful experience to collaborate with the plasma accelerator group at USC. Patric and Tom have always opened their doors for me and invited me to sit at their small round table to discuss the interesting physics of the plasma accelerator—using terminology that was totally strange for me just two years ago. It is always a pleasure to work with Efthymios (Themos) Kallos on the plasma

source experiment, to take data and analyze the mysterious results. I also appreciate him introducing me to Greek food, as well as Guitar Hero.

Aside from those people that directly related to my research, a number of other people influenced my life during the Ph.D. years. First of all, I would like dedicate my thanks to my parents with their endless love. Although they are at the other end of the earth, they are always there for support. I am also grateful that I met my husband Luo Zhicheng (Roy) here at USC. We came from the same hometown in China, we attended the same college in China, but we didn't know each other until we met at USC. I would like to thank Roy for his unlimited encouragement and understanding. Thank you for always being there with me, to both face the difficulties and share the happiness together.

Finally I would like to thank my colleagues and friends for sharing with me every memorable moment in graduate school.

Table of Contents

List of Figures

Abstract

Pulsed power technology is one of the tools that is used by scientists and engineers nowadays to produce gas plasmas. The transient ultra high power is able to provide a huge pulse of energy which is sometimes greater than the ionization energy of the gas, and therefore separates the ions and electrons to form the plasma.

Sometimes, the pulsed power components themselves are plasma devices. For example, the gas type switches can “turn on” the circuit by creating the plasma channel between the switch electrodes. Mini Back Lighted Thyratron, or as we call it, mini-BLT, is one of these gas type plasma switches. The development of the reduced size and weight “mini-BLT” is presented in this dissertation. Based on the operation characteristics testing of the mini-BLT, suggestions of optimizing the design of the switch are proposed. All the factors such as the geometry of the hollow electrodes and switch housing, the gas condition, the optical triggering source, etc. are necessary to consider when we design and operate the mini-BLT.

By reducing the diameter of the cylindrical gas path between the electrodes in the BLT, a novel high density plasma source is developed, producing the plasma in the

“squeezed” capillary. The pulsed power generator, of course, is inevitably used to provide the ionization energy for hydrogen gas sealed in the capillary. Plasma diagnostics are necessarily analyzed and presented in detail to properly complete and understand the capillary plasma. This high density plasma source (10^{19} cm^{-3}) has the potential applications in the plasma wakefield accelerator. The resonant oscillation behavior of the particles in plasmas allows for dynamically generated accelerating electric fields that have orders of magnitude larger than those available in the conventional RF accelerators.

Finally, the solid state switches are introduced as a comparison to the gas type switch. Pulsed power circuit topologies such as the Marx Bank, magnetic pulse compression and diode opening are used to accomplish the pulse generator design. Their applications for the transient plasma car engine combustion and bio-medical skin cancer cell treatments are also introduced.

Chapter 1: Introduction

1.1 Pulsed power system

Pulsed power is the term used to describe the technology of accumulating energy over a relatively long period of time and releasing it into a load in a short time interval (sometimes this process is called energy compression) to obtain a transient huge power. We can do a simple calculation to see the effect of the energy compression. If we have one Joule of energy in the energy storage system and we release this energy within one nano-second, we can achieve one Giga-Watt of instantaneous power.

Pulsed power was first developed during World War II for usage in Radar. Afterword, it was widely applied in particle accelerators, ultra-strong magnetic fields, fusion research, electromagnetic pulses, and high power pulsed lasers, etc. The pioneering roots of modern pulsed power were established by John Christopher (Charlie) Martin [Martin 1996] and his colleagues. And since the initiation of the IEEE Pulsed Power Conferences in 1976, engineering and physics standpoints have been adequately delineated in the pulsed power research. Nowadays, pulsed power technology has translated into people's daily life and plays roles in bio-medical therapy [Garon 2007, Schoenbach 1997],

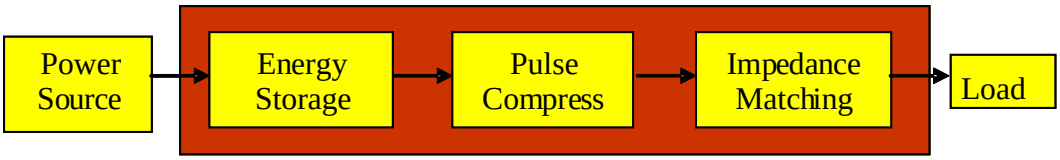

Figure 1.1 Block diagram of typical pulse generator

automobile ignition [Liu 2005, Wang 2005b], pollution control [Smulders 1998, D'Agostino 2008], food industry [Galindo 2008] and others.

The typical structure of the pulsed power system, as shown in Figure1.1, is composed of the power source, energy storage subsystem, pulse forming network, and the load impedance matching network. In order to produce an electrical pulse, first of all, we need to obtain a certain amount of the energy from the power supply. Once we turn on the power source, the energy is delivered to the energy storage components via the power charging circuit. The charging time for the energy storage is determined by the power source and charging circuit.

There are two major methods for storing the electromagnetic energy: energy stored in an electric field (capacitive storage), and in a magnetic field (inductive storage). The simplified way to calculate the energy W stored in the capacitor can be written as $W = CV^2/2$, wherein C is the capacitance of the capacitor, and V is the voltage on the two electrodes of the capacitor. The maximum energy density stored in the capacitor is not

only limited by the breakdown strength of the dielectric material, but is also limited by the capacitor package methods and the operation condition (such as working frequency, charging speed and voltage reversal). In another hand, inductive storage components are able to store the energy $W = LI^2/2$, wherein L is the inductance and I is the current flowing through the inductor. More specific, if we express the inductance L as:

$$L = \frac{\mu N^2 A}{l} \tag{1.1}$$

where A is the cross section of the magnetic flux loop, l is the length of the loop, N is the turn number of the inductor. And according to Maxwell function:

$$\begin{aligned} \nabla \times H &= I \\ I &= \frac{Hl}{N} \end{aligned} \tag{1.2}$$

The energy in the inductive storage can be expressed as:

$$W = \frac{LI^2}{2} = \frac{\mu H^2 lA}{2} = \frac{B^2 lA}{2\mu} \tag{1.3}$$

Thus the magnetic energy density in the inductive storage is $B^2/2\mu$ (J/m^3). As the same, the energy in capacitive storage is:

$$W = \frac{CV^2}{2} = \frac{1}{2} \times \frac{\varepsilon_0 A}{d} \times \left(Ed\right)^2 = \frac{\varepsilon_0 E^2 Ad}{2} \tag{1.4}$$

Thus, the energy density in the capacitive system is $\varepsilon E^2/2$ (J/m^3). In the aforementioned description, B is the magnetic flux density, μ is the magnetic permeability, E is the electrical field and ε is the dielectric permittivity. Therefore, the energy density in the inductive system is orders of magnitude greater than that of capacitive systems [Mankowski 2008].

Several considerations increase the design complexity of the inductive storage. First of all, since B is proportional to the conducting current, high current is needed for high energy density storages. Therefore, a cooling system is needed to dissipate the Joule heat generated by the large current. In addition, a shielding system may be required to avoid a leakage of the magnetic field which would affect the surrounding electronic devices. What is more, mechanical supports are needed to hold the magnetic coil against the magnetic forces. Therefore, although magnetic storage benefits the higher energy density capability, most modern pulsed power systems are still based on capacitive storage, and inductive storage is widely used as an intermediate storage unit. A good example will be the ignition coil for the spark plug in an automobile [Tang 2008].

There are multiple pulse forming network (PFN) types commonly used in the pulsed power, such as Marx Bank [Mallik 1999], Blumlein (transmission line type) pulse generator [Crouch 1972], magnetic pulse compression [Tang 2007], etc. Although the design topologies of the PFN are different, they each play an important role in boosting

output voltage by multiplying the input voltage and/or reducing the output duration time. In order to achieve a certain high output power or short pulse duration time, sometimes several PFN topologies are combined.

Impedance matching network typically exists between the pulse generator output and the load, maximizing the power delivery to the load and minimizing the energy reflections.

1.2 Review of pulsed power switches

High-power, high-voltage switching is one of the primary interest topics in most pulsed power system designs. Typically, the pulsed power switches are applied between the energy storage and PFN to transfer energy from relatively low power level to form higher power output. They are also used in the PFN as well, controlling the energy compression process. Therefore, the pulsed power switching is one of the main factors which not only determines the maximum energy transfer in the system, but also determines the speed of the energy transportation.

Based on the operation status, high power switches can be classified into two basic types: closing and opening switches. “Terms as ‘opening’ or ‘closing’ are used to describe which transitional state of the switch is controlled to achieve the desired circuit function.” [Martin 1990] In most cases, charge transportation through the previous medium requires

maintaining the switch closure to construct the conduction path. In comparison, opening switches are not used as widely as closing switches. They are typically used in the inductive system. In addition, on the basis of the property of the medium that is employed between the switch electrodes, the pulsed power switches can be classified as gas switches, solid state switches and liquid switches.

Although the specific terminology of the pulsed power switch is sometimes different, the parameters that are used to evaluate the switch performances have much in common. The regular switch parameters are described below, from the reference [Martin 1990]:

Hold-off Voltage - The maximum voltage that can be provided between the electrodes of the switch without breakdown. It is also called stand-off voltage, self-breakdown voltage or blocking voltage sometimes. The units are volts (V) or kilovolts (kV). The value of the hold-off voltage is determined by the medium property between the electrodes and the dielectric strength of the insulating envelope outside the switch. In some special cases, the switch is charged up rapidly in pulse mode with voltage higher than the DC hold-off voltage, which is called over-voltage.

Peak Current – The highest current conducting capability of the switch. The usual units are amperes (A), or kiloamperes (kA). It is limited by the medium conducting property and the geometry of the electrodes. Especially in the gas switch, the hollow structure of

the switch cathode improves the peak current. The hollow cathode mode [Pitchford 1995] of the pseudospark switch will be discussed in detail in Chapter 2.

dI/dt – The rate of the current change that can be applied without device damage. The usual unit is amperes per second (A/s). The limitation for this rate is imposed by the carrier formation rates, heat capacity and thermal conductivity of the switch itself.

dV/dt – The rate of the voltage change. The usual unit is volt per second (V/s).

Delay Time – The time interval between the application of a trigger command and the initiation of switch conduction. The usual units are second (s), micro-second (μs) or nano-second (ns). This time interval is composed of processes which involve the generation of the initial charge carriers and the pre-breakdown phases to establish conducting channels between the electrodes. In addition, the inductance of the switch itself and the pulsed power system also increases the delay time of the switching.

Jitter – The statistical variations of the delay time. This time is usually measured in ns or μs. Since sufficient energy is required to accelerate the carriers and transport them to the gap to establish "switch-on" and sustain the conduction. Because the initial charge will have some initial velocity distribution, some of the carriers will cross the gap later than others, resulting in switching "jitters". Thus, the initial conditions are very important and some switches use "keep alive" discharges, lasers or electron beams to reduce jitters.

These devices help to insure consistent behavior of the initiation process, particularly when timing is critical.

Recovery Time – The time for the recovery of the dielectric properties of the switch so that voltage can be reapplied at some rate (dV/dt). The recovery process relates to the plasma kinetic characteristics of the conducting medium which include the charge density, mobility, temperature, recombination, attachment, mean free paths, and applied fields, etc.

Forward Drop – The voltage drop across the switch impedance during the “turn on” phase. When the switches work for high current or high frequency operations, the heat problem caused by the forward drop becomes serious, and a cooling system is necessary.

Repetition Rate – The rate at which the switch can be operated without degradation of characteristics. The usual units are Hertz (Hz) or kilohertz (kHz). The rate is limited by the switch recovery time and forward drop.

Life Time – The number of operation times, sometimes called “shots”, beyond which the switch cannot work properly.

The definitions of those switch parameters above could be a guide when we choose and design switches for the real applications. These parameters are commonly mentioned for switch characterization evaluations.

1.3 Brief introduction to the particle accelerators

One of the major applications of pulsed power is tooling for high energy physics research. In order to explore the fundamental forces of nature, modern particle accelerators are designed and built. Those accelerators provide strong electrical fields to accelerate charged particles such as electrons and protons to high energies, and then to smash them against each other at nearly the speed of light. By observing the behavior of the products of those collisions, the elementary constituents of matter can be analyzed and new fundamental laws may be found.

In 1932 the world's first cyclotron was built by Ernest O. Lawrence. It was a mere 4 inches (100 mm) in diameter [Lawrence 1932] and provided 1 MeV acceleration energy. The latest world's-largest and highest-energy particle accelerator, the Large Hadron Collider (LHC), is built in Geneva, Switzerland, and operates underground in a 27 km long tunnel [LHC]. Each proton flying around the LHC will obtain an energy of 7 TeV. So when two protons collide, the collision energy will be 14 TeV. The price tag for LHC is between 5 and 10 billion dollars. On 10 September 2008, the proton beams were successfully circulated in the main ring of the LHC for the first time. On 19 September 2008, the operations were halted due to a serious fault between two superconducting bending magnets. The operation of LHC is proposed to resume in late 2009. Figure 1.2 shows the photos of Lawrence's table-top accelerator and supper huge LHC.

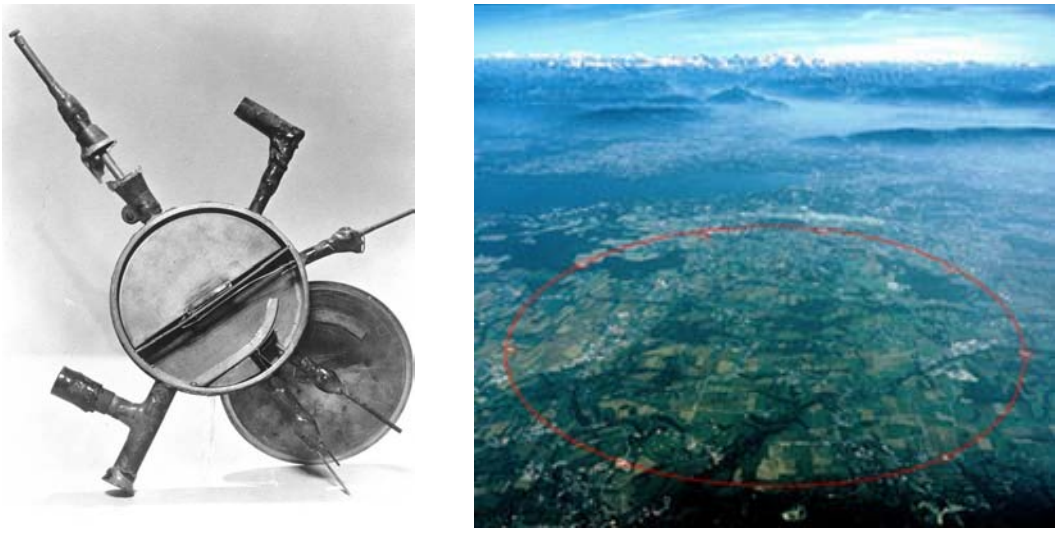

(a) (b)

Figure 1.2 (a) The first cyclotron, invented by Ernest O. Lawrence. The diameter of the round chamber is 10 cm. (b) Aerial view of the underground LHC. The diameter of the circle is 9 km.

During the past 70 years, several generations of accelerators and colliders have been developed. The size, cost and complexity of the accelerators has increased, along with the rise of the energy frontier. The progress of the accelerator energy over the past several decades is depicted in Figure 1.3 [Panofsky 1999]. The fundamental limits on current accelerators come from the properties of the materials used in the vacuum cavity. There is a “damage threshold”, beyond which the strength of the electromagnetic field will strip electrons off the cavity wall to interact with the accelerated particles, and even cause

instantaneous electrical breakdown on the walls [Braun 2003] and long-term thermal cyclic fatigue [Pritzkau 2002].

1.4 Brief introduction about the plasma accelerators

Plasma-based accelerators have attracted interest as a novel acceleration scheme that could boost the energy of an incoming beam over very short distances [Bingham 2007]. What is more, this new type of accelerator excites electrical field orders of magnitude

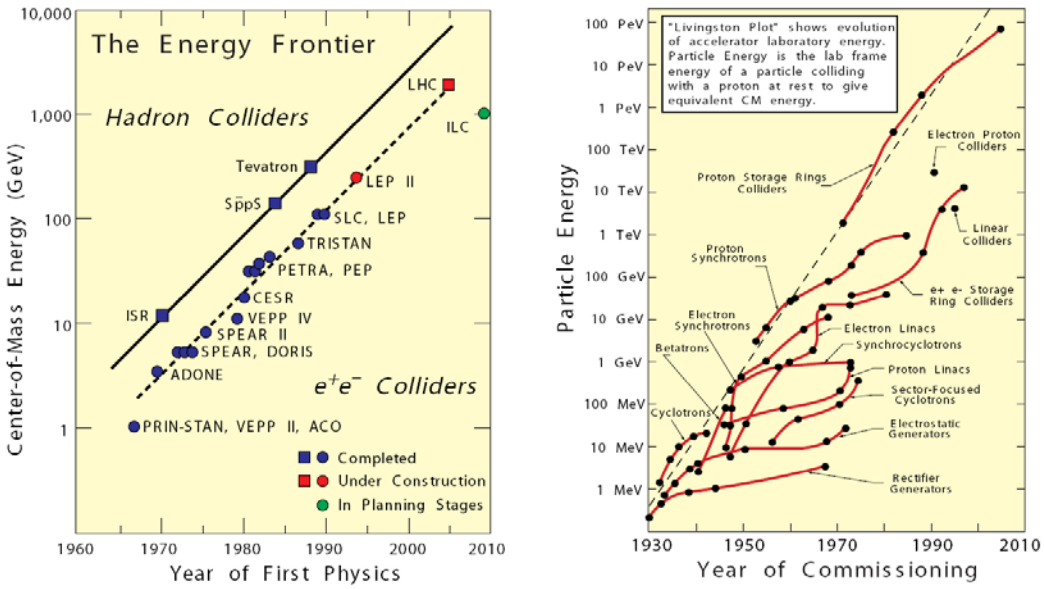

Figure 1.3 The Livingston curve shows the progress of the energy of various accelerators with time.

higher than the conventional accelerator does, without mechanically damaging the cavity. Large accelerating gradients can be reached because plasmas can support 10 – 100 GV/m electric fields. A simple estimate for the strength of the electric field oscillation amplitude can be made by using Gauss's law:

$$\nabla \cdot \vec{E} = \frac{\rho}{\varepsilon_0} \tag{1.5}$$

Assuming a one – dimensional plane wave perturbation of the charge density,

$$\rho = e_0 \, \Delta n \, e^{+ik_p z} \tag{1.6}$$

where e_0 is the electron charge, Δn is the plasma density perturbation, and the plasma wavenumber is

$$k_p = \frac{\omega_p}{c} \tag{1.7}$$

where c is the speed of light in vacuum and ω_p is plasma frequency which is given by

$$\omega_p = \sqrt{\frac{e^2 n_0}{\varepsilon_0 m}} \tag{1.8}$$

The electric field perturbation is

$$\vec{E} = \hat{z} \, E_0 e^{+ik_p z} \tag{1.9}$$

For a density perturbation on the order of the neutral plasma density, $\Delta n \sim n$, the electric field amplitude E_0 is then roughly

$$eE_0 \sim mc\omega_p \sim \sqrt{\frac{n_0}{10^{16}\, cm^{-3}}} \times 10 \frac{GeV}{m} \tag{1.10}$$

For a plasma with a neutral density $n_0 = 10^{18}$ cm^{-3}, equation (1.6) indicates that an accelerating electric field (wakefield) of 100 GV/m could be supported by the plasma. This electric filed is orders of magnitude higher than the ones sustained in conventional accelerator structures (~100 MV/m) [Wilson 2004].

In the plasma accelerator scheme, as shown in Figure 1.4 [Kallos 2008a], the driven electron beam or laser beam is injected into the pre-ionized plasma and repels the electrons in the plasma away. Since the ions are much heavier than the electrons, they remain stationary while the electrons are moving. The repelled electrons will be drawn back by the positive charges, overshoot the axis, and set up a charge density wave oscillation behind the beam. The electrical potential difference on the axis caused by the dynamically charged density distribution creates a very strong electric field that propagates at the velocity of the beam. As a result, if a witness electron beam is placed at the proper phase with the plasma wakefield resonance, it will experience this accelerating field and be propelled to high energies. The charge distribution resonance is reached when the plasma wavelength $\lambda_p = 2\pi c/(n_e e^2/\varepsilon_0 m_e)$ is tuned by controlling the plasma

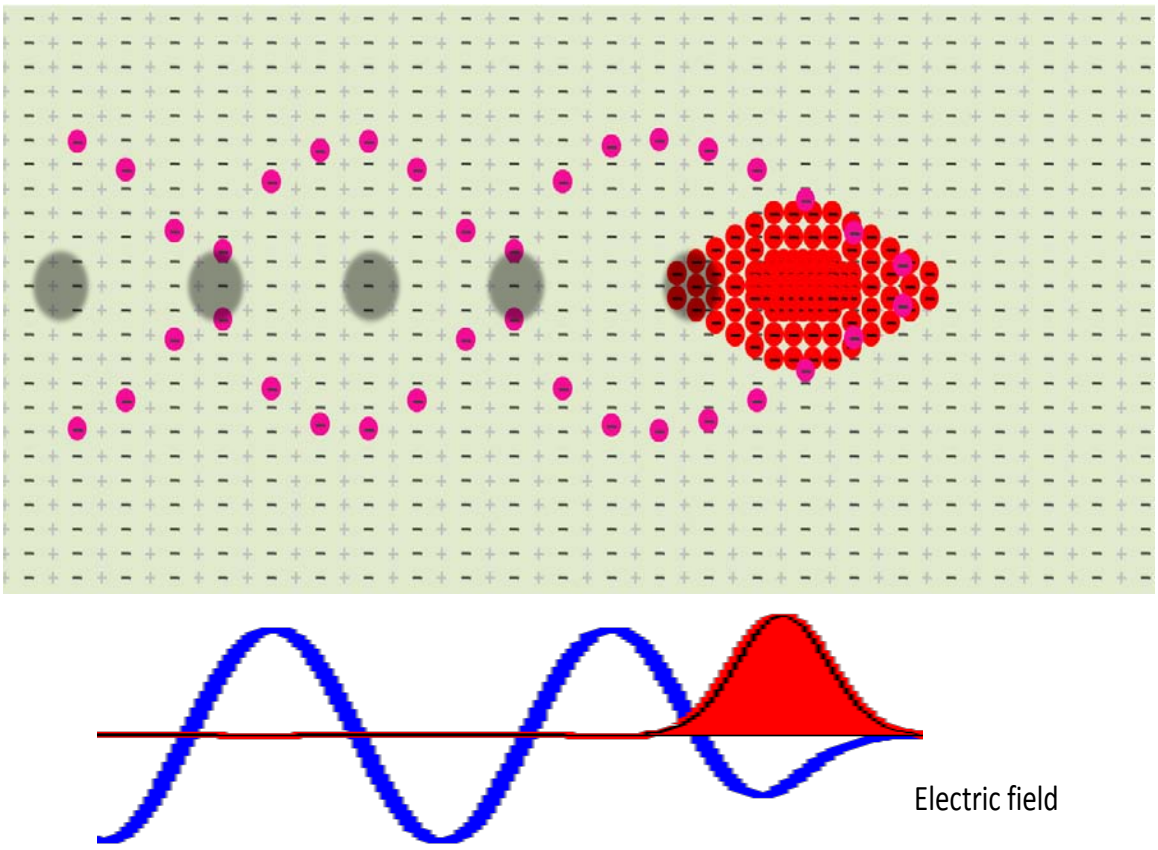

Figure 1.4 The schematic of a plasma accelerator.

density n_e. Such resonant experiments require a reliable and controllable plasma source at densities between 10^{16} and 10^{19} cm^{-3}.

The most common types of plasma-based wakefield accelerators are laser-driven, which are known as laser wakefield accelerators (LWFA) [Mangles 2004, Geddes 2004]; or particle-beam-driven, which are known as plasma wakefield accelerators (PWFA) [Blumenfeld 2007]. The generation of a radially parabolic plasma density profile is

important for the LWFAs in order to extend the acceleration length many times over the short Rayleigh length of the drive laser beam. The plasma channel also compensates for the laser beam defocusing caused by ionization-induced refraction [Gutler 2002] in a partially ionized gas. On the other hand, in PWFAs operating in the nonlinear blowout regime, the plasma ion column provides the focusing for the electron beam [Clayton 2002, Muggli 2004], and uniform plasmas are sufficient. A notable breakthrough in this field was reached at the Stanford Linear Accelerator Center where some electrons in a single bunch gained 42 GeV over 85 cm of plasma [Blumenfeld 2007]. In the PWFA, the wakefield amplitude scales with the square root of the unperturbed plasma density [Lu 2005], and therefore, wakefields driven by short bunches in high-density plasmas provide larger accelerating gradients. In addition, multi-bunch PWFA techniques have been proposed in which a train of drive bunches resonantly excites the wakefield, and can be sampled by a trailing witness bunch [Geddes 2005, Kallos 2008b]. In those schemes the accelerating gradient is optimized when the wavelength of the plasma oscillations matches the separation between the drive bunches, which are produced, for example, using an IFEL [Kallos 2005] or a mask technique [Muggli 2008].

The plasma-based accelerators overcome the field gradient limitations (greater than 150 MV/m causes the cavity wall breakdown). However, it should be pointed out that the plasma accelerator itself dose not provide energy, it is merely an energy transformer to

transfer the energy of an existing beam to a trailing beam. As such, the traditional accelerators are still needed to provide the initial energy to the driven beams, and the plasma accelerator will then extend the energy of the witness beams to a higher level.

1.5 The scope of the thesis

This thesis will introduce the research on the plasma devices and their applications in the pulsed power, high energy physics, and biomedical applications, etc. In chapter 2, the topic focuses on the design and characterization of the gas-type hollow cathode switch, the Back Lighted Thyratron. In chapter 3, the explorations on the development of the high density hydrogen plasma source will be introduced. In chapter 4, discussion on the pulsed power switch will extend to the solid state switches, and circuit designs with these switches will be introduced. Summary of this thesis work will be demonstrated in Chapter 5.

The work presented in this dissertation is a combination of several topics of plasma device designs and pulsed power designs. The experimental setups, diagnosis and result discussions of each device are stated in detail in the respective chapters. So, after acquiring the general knowledge from this chapter, each chapter in the following can be read independently if interest is in a particular topic.

Chapter 2: Back Lighted Thyratron

Gas type switches are widely used in high voltage applications that can realize the "switch-on" status by ionizing the gas and forming a low resistance channel. An example of the gas type switch is a spark plug, which conducts the current while the spark (actually it is an arc) is produced at atmosphere pressure in a car engine. This switch operates very reliably at low current, but it has limitations related to lifetime for high current operation. Thyratron switches are capable of handling tens of kilovolts and tens of kiloamperes at the cost of large size and significant housekeeping power to maintain high temperature at the thermionic cathode. Pseudosparks [Christiansen 1979] are gas type high voltage high power switches with an essentially cold cathode which has similar hold-off voltage and peak current capability as the thyratron but significantly reduced size and weight. With low pressure gas (hydrogen is the typical gas type) filled, pseudosparks work at the left hand side of the Paschen's curve [Paschen 1889] (see Figure 2.1) to achieve high hold-off voltages. The back lighted thyratrons belong to the pseudospark family with optical triggering system.

The initialization of the pseudospark cathode emission is provided by a hollow-cathode mode when the anode potential penetrates into the inside of the hollow cathode cavity to

multiply the generation of electrons. Subsequently, this mode transits into the self-heated super-emissive mode. A huge number of the electrons is emitted from the field emission when the anode potential drops in the plasma sheath along the hollow cathode, where the electrical field reaches more than 10^6 V/cm (the plasma sheath thickness is typically less than 100 μm) [Boeuf 1991, Hartmann 1988]. The re-deposition of the cathode materials [Anders 1993, Anders 1995] combining with multi-channel electrode designs [Naweed 1999, Frank 2007] prolongs the lifetime of the pseudospark up to 10^9 shots for the medium power switch applications [Tkotz 1995].

The "switch-on" and "switch-off" status is controlled by the triggering system. The triggering will provide a certain number of seed-electrons that will finally form a gas plasma channel inside of the switch and realize the "switch-on". When the triggering is off, the gas holds off the high voltage without breakdown for "switch-off" status. In the traditional pseudospark, the electrical triggering system is integrated into the switch to deliver a high voltage pulse. The field emitted electrons generated from the pulse, work as the "seed" to start the gas discharge. Nevertheless, an optically-triggered version of the pseudospark switch has been developed during the recent decades, which is called the Back-Lighted Thyratron [Kirkman 1986] (BLT). Instead of the pulse induced "seed", photoelectrons, which are generated from the interaction between the UV light and the

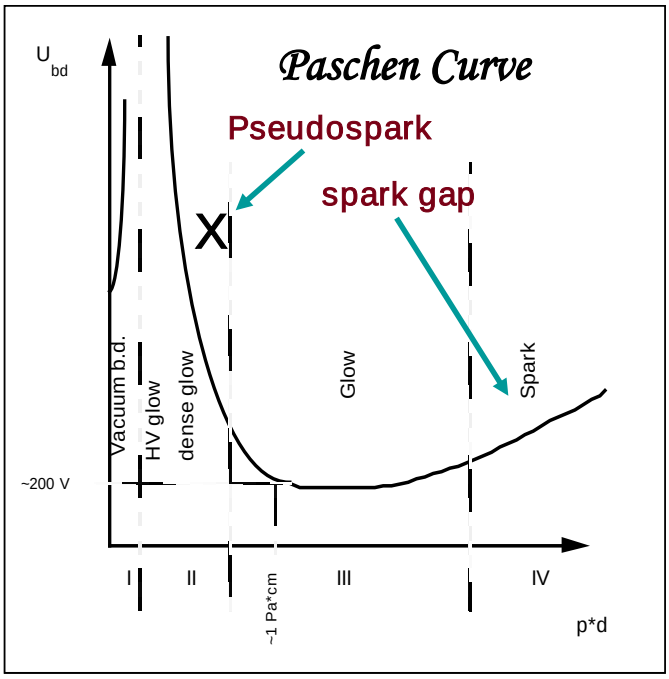

Figure 2.1 Paschen curve indicates the breakdown voltage of the gas as a function of the product of gas pressure p and the voltage drop distance d. Pseudopsark works at the left hand side of the Paschen curve where the gas breakdown voltage increases as the p × d decreases.

metal electrodes lead to “switch-on” status. By excluding the electrical trigger components in the BLT, the overall weight and size of the switch are greatly reduced.

In this chapter, the development of the mini-BLT for portable ignition applications is illustrated. The mini-BLT is 15 cm^3 in volume, which is about 20 times smaller than the traditional pseudospark. In section 2.1, the super-emissive hollow-cathode mode is introduced. Section 2.2 describes the setup of the experimental system for switch characterizations. In section 2.3 the operational characteristics of the switch such as the

hold-off voltages, delays and jitters are discussed. In section 2.4, the integration of the mini-BLT to a pulse generator for transient plasma ignition applications is presented. Finally, the results are summarized in section 2.5 and future work is stated in section 2.6.

2.1 Super-emissive hollow-cathode mode

Hollow cathode, as named, is the plane electrode with a central aperture hole and cavity body, as shown in Figure 2.2, charged with a negative potential. Several theoretical models have been proposed to explain the mechanism of the supper-emissive phenomena in the hollow cathode, which result in the high current conducting capability of the BLTs. Understanding the onset of the breakdown and the subsequent electron emission from the interior of the hollow cathode guides the switch optimized design.

The gas ionization in the hollow cathode provide the electron and ion source which should satisfy the particle continuity equation:

$$\frac{\partial n_{e(p)}}{\partial t} + \nabla \cdot n_{e(p)} v_{e(p)} = S \qquad (2.1)$$

where $n_{e(p)}$ is the electron or ion density respectively, $v_{e(p)}$ is the electron or ion mean velocity, S is the ionization source term which represents as the number of ionization event per unit time in the unit volume.

With the Poisson's equation:

$$\nabla^2 V = -\frac{|e|}{\varepsilon_0}(n_p - n_e) \tag{2.2}$$

and charged particle flux, the plasma can be described and numerically solved with the aid of the computer simulation. The flux equation is written below:

$$n_{e(p)} v_{e(p)} = n_{e(p)} \mu_{e(p)} E - \nabla(n_{e(p)} D_{e(p)}) \tag{2.3}$$

where $\mu_{e(p)}$ is the mobility of the particle and $D_{e(p)}$ is the particle diffusion coefficient.

Computer simulation by using 2D-hybrid fluid-Monte Carlo model [Boeuf 1991], was processed to describe the initiation phases of the hollow cathode. A two-dimensional cylindrically symmetrical geometry is used in this model. The electrons and positive ions' time-space dependent fluid equations and Poisson's equation are solved self-consistently.

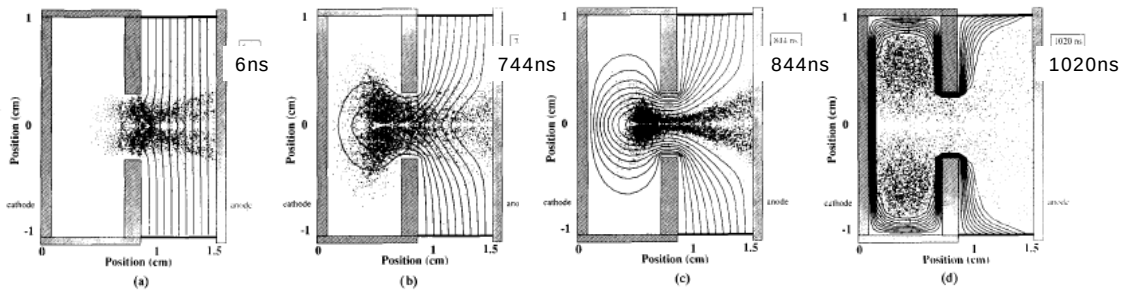

Figure 2.2 Contour of the constant potential at different phases of the hollow cathode discharge from Monte Carol simulation. The plasma is also shown as the black dots. [Boeuf 1991]

Figure 2.2 shows the electrical potential distributions in the hollow cathode at four different phases during the discharge. The Townsend discharge phase (Figure 2.2a) happened at the very beginning when the potential is almost uniformly distributed between the electrodes. After the triggering creates the "seed" electrons, they are extracted by the electric field and get accelerated. The accelerated electrons collide with the gas between the electrodes and cause avalanched secondary electron emissions. Plasma formation phase (Figure 2.2b) happens successively when the accumulated ion-space-charge leads to the distortion of the electric field. Then, the potential starts to penetrate into the cavity of the cathode and the electrons are slowed down since the field in the main gap is decreased. Figure 2.2c, d demonstrates the onset of the hollow cathode effect when the plasma enters the back of the hollow cathode and compresses the thickness of the ion sheath along the cathode surface. The thickness of cathode sheath d_c relates to the electron density n_e and the potential drop between the sheath, which is describe as:

$$d_c = \left(\frac{2\varepsilon_0 V}{e n_e} \right)^{1/2} \tag{2.4}$$

In chapter 2.4 the bulk plasma density is measured around 10^{14}-10^{15} cm^{-3}. If we choose 20 kV applied voltage at the switch, the thickness of the sheath is around 60 μm. Then the

huge field strength up to 3×10^6 V/cm is created which enhances the electron field-emission from the cathode cavity.

In addition, W. Hartmann and M. A. Gundersen [Hartmann 1988] proposed in 1988 that the cathode surface is heated up by the intense ion bombardment with a power density of the order of 25 MW/cm^2, therefore, the temperature at the thin layer of the cathode surface can increase to nearly 3000 K, which is above the melting point of the electrodes material: Mo (2893 K). Although the hot layer only exists for a short time (around 30 ns), it acts like a thermionic cathode to release dense electrons via the field-enhanced thermionic emission [Murphy 1956]. Soon after, the surface heating speed was questioned in this hypothesis. Anders and his colleague [Anders 1993, Anders 1994] argued that the experimental maximum power density was too low to heat up the cathode surface fast enough for thermo-field emission. They neglected the minor contribution of the cathode self-sputtering due to its low sputtering rate. Instead, they believed that when the virtual plasma anode gets in close proximity to the cathode, the ion bombardment heats up the micro-tips or micro-protrusions on the cathode surface, where the bulk plasma virtual anode is within a few tens or hundreds of micro-meters from the cathodes, rather than milli-meters distance away as the real anode. As a result, the Joule heat in the micro-protrusions creates localized high temperature and field strength, which forms the

explosive emission spots. Many of these spots are distribute on the cathode and initialize the dense electron emission.

More discussions about the process of the electron super emission in hollow cathode are published, looking into the physical insight of the phenomena. Most of the theory explains the possible mechanism that in some ways increases the particle collisions to produce high gas ionizations rate. For example, self-sustained self-sputtering [Anders 1995], which is lead by the ion return to the cathode, enhances the secondary electron generation. Also, the pendulum motion [Eichhorn 1993, Kim 2008] of the fast electrons, the stepwise ionization and cathode bombardment by photons and metastables [Kim 2006, Bauer 1990] are believed to be one or some of the possible reasons to produce higher ionization collision probability and electron secondary emissions.

2.2 BLT design and setup

From the previous introduction, we know that the BLT is developed from the pseudospark with the variation of the triggering method. The mini sized BLT (mini-BLT) was designed and built at University of Southern California. The schematic of the dismountable mini-BLT is shown in Figure 2.3. The electrodes are made of oxygen-free, high-conductivity (OFHC) copper tubing capped with molybdenum (Mo) studs (6.3 mm

in diameter, 4 mm thick in total). For the super-emissive mode configuration, 3 mm aperture holes are drilled in both studs. Adjustable screws set the distance between the two electrodes. Ultra-violet (UV) light from the UV laser or flash lamp passes through a fused quartz window to strike the BLT cathode surface. The insulated housing is simply a borosilicate glass cylinder (76 mm long and 12.7 mm in diameter) and it is o-ring sealed to Ultra-Torr vacuum fittings. Figure 2.4 shows a photo of different versions of the BLTs and pseudospark. Compared to the pseudospark, the size of the latest version of the mini-BLT is shrunk down more than ten times.

The mini-BLT prototype is connected to a vacuum chamber. Once the valves between the switch and the vacuum chamber are closed, the pressure is fixed during the experiment. Figure 2.3 also illustrates the test circuit for the mini-BLT. A negative DC high voltage is applied to the cathode side of this device. A 6 nF capacitor bank is stacked around the switch in a compact axially symmetric configuration to minimize the system inductance. A 2.2 Ω stack resistor is in series with the switch to dampen the circuit oscillations. By measuring the period of the voltage oscillation on the resistor, $T = 2\pi(LC)^{1/2}$, approximate 80 nH total system inductance is estimated. Discharge current is measured by Pearson Current Probe. A commercial high voltage probe with 1:1000 attenuation ratio is used to measure the voltage drop across the resistor.

A 355 nm UV Laser (Continuum Powerlite 8000) is used to study the trigger delay and jitter for the mini-BLT. The laser energy is measured by a laser power meter. A UV flash lamp (EG&G FX265) was also tested as the optical triggering source for the mini-BLT.

2.3 Hold-off voltage testing

To understand and optimize the design of mini-BLTs, several factors that will affect the hold-off voltages are investigated. Figure 2.5a illustrates the hold-off voltages of the mini-BLT filled with helium or hydrogen. The separation of the electrodes is set at 2 mm. The switch hold-off voltage decreases as gas pressure increases. When the switch is filled with helium, hold-off voltages up to 40 kV are achieved at 800 mTorr pressure. Due to owing lower ionization energy in hydrogen (first ionization energy of hydrogen is 13.6 eV, of helium is 19.8 eV), the same hold-off voltage can be achieved with a hydrogen-filled switch, but at pressure <400 mTorr. Although helium benefits higher hold-off voltages than hydrogen, hydrogen is still the most widely used medium in the commercial available gas-type switches. The vacuum brazing technology and hydrogen reservoir can guarantee the desired gas condition for switch operations. However, in the real world, the helium atom can gradually leak out of the dielectric envelop and end the switch life before the switch electrodes die out.

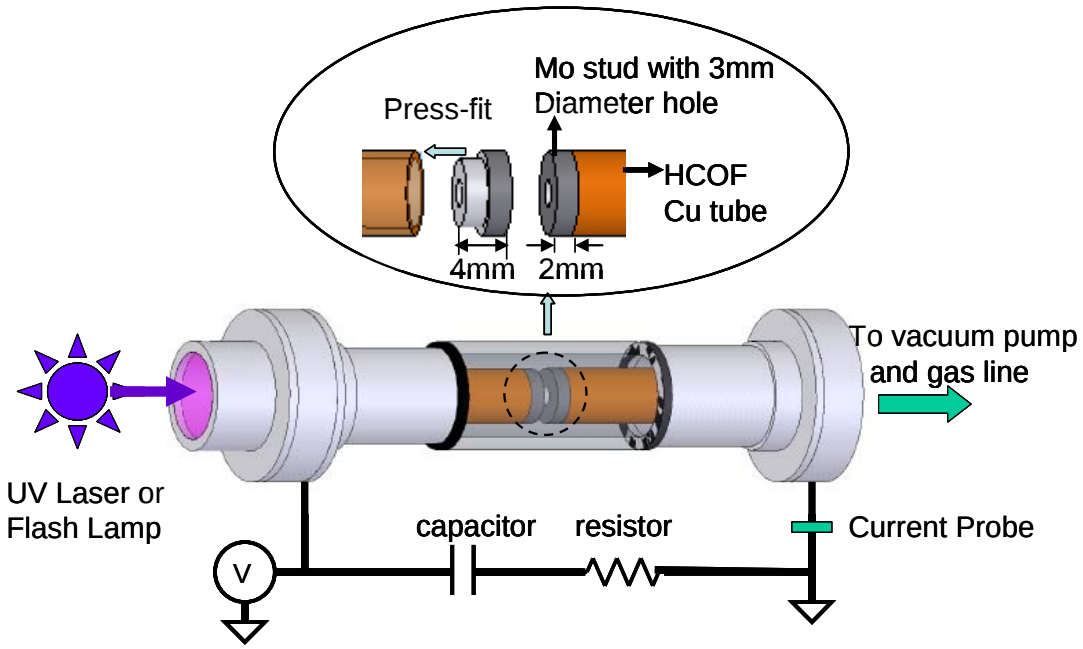

Figure 2.3 Schematic of the mini-BLT and the testing circuit. Negative high voltage is charged at the cathode of the switch. UV optical source strikes on the cathode side of the switch for triggering control via passing through the quartz window. Molybdenum studs with central holes are press-fit into the HCOF tube to structure the hollow cathode. Vacuum pump and gas line are needed for gas pressure controls in this prototype.

Figure 2.4 Photos of the Pseusopark and BLTs. Compared to the pseudospark, the effective size of mini-BLT is reduced by more than ten times.

According to Paschen's law, higher hold-off voltage can be obtained in a smaller p × d value (pressure × distance) on the left hand side of the curve minimum. Therefore, decreasing the pressure is a normal way to increase the hold-off voltage when the electrode distance is fixed. However, the operation at a pressure below 200 mTorr results in vacuum breakdown [Jiang 2005], which causes strong erosion of the electrode surface and significantly reduces the switch lifetime. Therefore, no data is taken when gas pressure is under 200 mTorr. When gas pressure increases around 1000 mTorr, the glow discharge occurs, which was well studied and is not the main interest in this thesis.

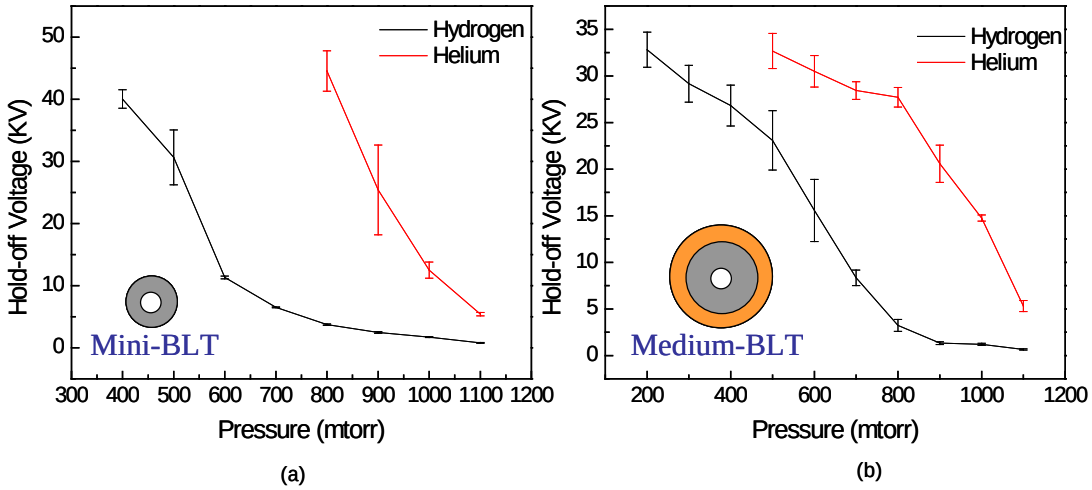

Figure 2.5 (a) Mini-BLT (b) Medium-BLT hold-off voltage as a function of gas pressure when filled with hydrogen and Helium. The top view of the switch electrodes are shown at the lower-left corner of each graph. Mini-BLT has pure Mo hollow electrode surface. Nevertheless, the electrode surface of medium-BLT is composed of Mo (grey part) surrounded by the copper (orange part) in a concentric circular way.

Figure 2.5b is the hold-off voltage curve for the medium-BLT, whose dimensions are larger than the mini-BLT. The electrode of the medium-BLT is constructed so that a 19 mm outside diameter copper ring surrounds a Mo ring (with outside diameter of 12.7mm) with a 3 mm-diameter concentric aperture hole. Hold-off voltages higher than 30 kV are observed in the medium-BLT, however, compared to the mini-BLT, it requires lower pressure for the same hold-off voltage. For example, in mini-BLT, 900 mtorr helium is enough to hold off 30 kV, while 600 mtorr is necessary for medium-BLT. The larger amount of micro-protrusions on the electrode surface of the medium-BLT may cause higher break-down probabilities and would need lower pressure for compensation. Moreover, since the Mo stud is inserted into the copper, the electrode surface has a micro groove at the boundary of those two materials. Therefore, the field emission from the boundary also reduces the hold-off voltage capability of the medium-BLT. Nevertheless, switches with larger cathode surfaces result in higher current handling ability if the same current density is sustained between the electrodes. Large electrode surface area is a must for ultra high power applications. The mini-BLT introduced here is suitable for power applications under 200 MW.

It is necessary to point out that air breakdown outside the glass housing occurs when the applied voltages exceed 45 kV during the mini-BLT operations. Increasing the overall

length of the insulator housing can solve this problem if higher hold-off voltage is desired, although that will increase the size of the switch.

In addition to the dependence of the hold-off voltage on the gas type and gas pressure, the electrode separation distance also affects the hold-off voltages. According to the experimental observations (see Figure 2.6), an electrode separation of 2 mm results in the maximum hold-off voltage of the mini-BLT (for a fixed helium pressure of 800 mTorr), as shown in Figure 2.6. Low (<20 kV) hold-off voltage is obtained when the separation is less than 2 mm. This is caused by vacuum breakdown where local field emission and cathode evaporation occurs from electrode surface micro-protrusions, which is harmful for the switch lifetime. As the separation increases beyond 2 mm, the hold-off voltage decreases, following Paschen's Law prediction.

Nevertheless, some deviations from Paschen's Law are observed for the hollow cathode break-down curve. The reason for this is that before the high-current break-down happens in hollow cathodes, the parallel electrical field between the electrodes is distorted by the apertures. The potential curve penetrates into the hollow cathode, causing the effective anode to cathode distance, $d_{eff,}$ to be longer than the real electrode separation distance [Pak 1992]. In addition, during high voltage hold-off, the electron impact excitation and ionization are not the only effects. Ion impact ionization also significantly contributes to

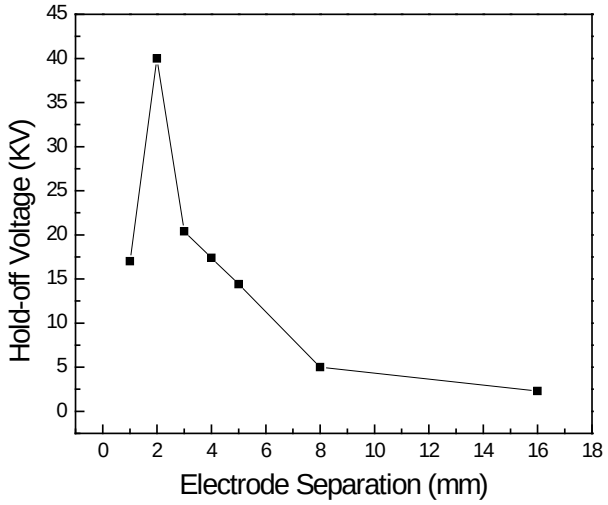

Figure 2.6 Hold-off voltages as a function of electrode separations in 800 mTorr Helium. The variation of the hold-off voltages is within 10% except for the peak point at 40 kV, whose error bar can be referred to Figure 2.5.

ionizations. In helium, the cross section for ion impact ionization exceeds that for electron impact at energies >200 eV and increases for higher particle energies.

The hollow-cathode emission requires d_{eff} longer than particle mean-free-path to form ionization collisions along particles transportation. The mean-free-path of helium ion is around 2.2 mm in 800 mTorr of helium, estimated by

$$\lambda = \frac{RT}{\sqrt{2}\pi d^2 N_A P} \tag{2.5}$$

in which d is the helium atom diameter, p is the gas pressure, N_A is the Avogadro's number, T is the temperature, R is the gas constant. Therefore, the real electrode separation is set at 2 mm, which optimizes the high hold-off voltages and guarantees that the supper emission happens simultaneously.

Electrode geometry specifications are another essential issue for the mini-BLT. The potential penetration increases with increasing cathode hole radius and decreases with cathode thickness [Pak 1992, Lin 1995]. Smaller cathode aperture radius or larger cathode thickness effectively reduce the pd product and cause the breakdown relationship in hollow cathode to more closely represent Paschen's law. When the cathode aperture radius is smaller than the mean-free-path of the ions, the number of ionization collisions in the radial direction decreases a lot, which reduces the amount of electron emissions. Moreover, when the cathode thickness exceeds 5 mm, breakdown is caused by electron avalanche occurring at the front face of the cathode instead of inside the cathode cavity, which also decreases the electron emissions. So, in conclusion, on one hand, thick electrodes with small aperture radii lead to high hold-off voltages. On the other hand, the diameter of the aperture should be comparable to the electrode separation to initiate the super-emissive mode [Bochkov 2000]. Considering these factors, a hole of 3 mm in radius is fabricated on the molybdenum studs and the thickness of the studs is chosen as 4 mm.

2.4 Optical triggering

In general, “seed” electrons are required to initialize the breakdown in the gas switch. There is a threshold in the amount of the “seeds”, beyond which the seeds overcome the recombination and avalanche the ionization. 10^9~10^{11} seed electrons are believed to be the critical number to finally initialize the discharging event both from the theoretical [Boeuf 1991, Cetiner 2008] and experimental [Mehr 1995] studies. Electrical triggering is widely used to obtain electrons through field emission, but the triggering system takes up space and increases the overall size of the switch. Optical triggering is another effective way to control the switch without complex elements. UV light strikes on the molybdenum cathode and produces photoelectrons to initialize the discharge in the BLT.

The switch delay is defined by the time interval between the on-set of the optical trigger and the load current rise to 1% of the peak value (See Figure 2.7a). This definition does not include the trigger instrumentation delay. Only the time delay between the launch of the light and current is considered. A fast response photodiode (<1 ns response time) is used to identify the optical triggering which is the blue curve in Figure 2.7a. Minimum delay of 30 ns ± 2 ns is achieved when a 355 nm laser pulse (>70 mJ/pulse) incidents at the back surface of the cathode, as shown in Figure 2.7b.

A criterion electron density is necessary to reach in the hollow cathode to switch over to the highly conducting phase, where [Anders 1993]

$$n_e \geq n_e^{cr} = \frac{2\varepsilon_0}{eU_c}\left(\frac{E_c}{\beta}\right)^2 \qquad (2.6)$$

where E_c^{cr} is the critical fild strength at the cathode surface. In the case of tungsten, E_c^{cr} ~1×10^{10} v/m and n_e^{cr} ~ 5×10^{13} cm^{-3}. The higher energy optical pulses produce more photoelectrons during the 5-7 ns optical pulse duration, resulting in shorter time to produce the criterion from the secondary avalanch, therefore, shorter delay and less jitter is obtained.. In comparison, electrical triggering methods, based on charge-injection and surface discharge [Frank 1988], usually lengthen the switch delays by more than one order of magnitude, and produce more jitter than this UV laser trigger.

A flash lamp (EG&G FX265) was also used to trigger the mini-BLT, but the delay and jitter are in the range of several hundred nanoseconds to several microseconds. It has been observed that as low as 50μJ/pulse optical energy from the flash lamp is capable of triggering the switch.

Switching delay and jitter are also affected by the gas pressure [Jiang 2005] due to shorter mean free path of the particles. As a result, shorter delay and jitter can be obtained in higher pressure.

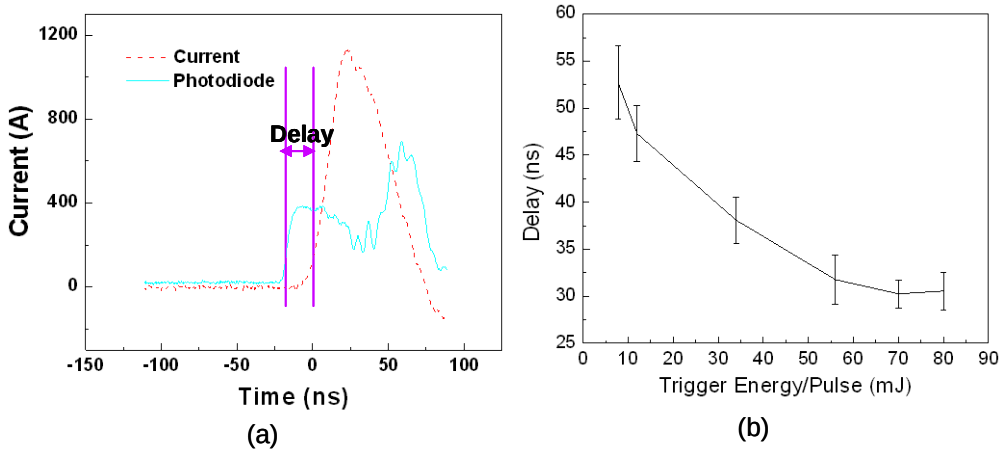

Figure 2.7 (a) Fast-response photodiode is used to detect the on-set of the optical trigger. The time difference between the optical trigger (solid curve) and the beginning of the current flowing (dotted curve) is defined as the switch delay. The photodiode signal distortion is caused by the high voltage pulse noising, however, the rising edges of the current and photodiode are clear enough to indicate the delay time.
(b) Delay and jitter of the mini-BLT with 800 mTorr helium, as a function of the 355 nm laser triggering energy. Minimum delay is 30 ns ± 2 ns. Each data point is the average of 20 measurements. Optical energy less than 20 mJ/pulse is obtained from a Continuum Minilite laser, and optical energy larger than 20 mJ/pulse is obtained from a Continuum 8000 YAG laser. The wavelength of both lasers is 355 nm.

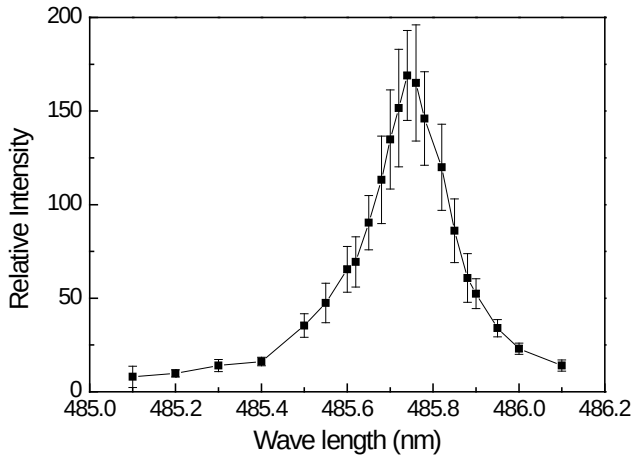

Figure 2.8 Spectrum of hydrogen beta line from the BLT discharge. 1.8Å FWMH of the Hβ line is corresponding to about 9×1014cm-3 electron density. 1 eV electron temperature is derived from the Hβ line to background intensity ratio.

The experiments were conducted at 10 Hz, as higher operation repetition rate is limited by the laser output repetition rate. Nevertheless the mini-BLT is expected to be capable of operation at repetition rates in excess of 10^3 Hz [Bickel 1991] with appropriately designed circuitry and optical triggering.

In order to diagnose the plasma inside of the switch when it operates, a monochrometor with 0.1nm resolution was used to detect the discharge spectrum in the mini-BLT along the axis. The light emission of the discharge inside the mini-BLT is coupled into the spectrometer, and the H_β line Stark broadening [Griem 1974] is used to calculate the plasma density. An example of a measured spectrum is shown in Figure 2.8. The average plasma density is calculated to be 9×10^{14} cm^{-3} when the peak discharge current is 3.24 kA. This is close to the density of 1×10^{15} cm^{-3}, which was observed in the larger BLTs [Bauer 1990]. The details of the spectroscopic diagnosis will be discussed in Chapter 3.

2.5 Applications

The switching performances of the mini-BLT are tested in the compact RLC testing circuit (see Figure 2.3). The typical voltage and current waveforms are measured and shown in Figure 2.9.

The polarity of the current (dash line) is reversed on purpose to distinguish the current waveform from the voltage waveform. After the 6 nF capacitor bank is charged with 27 kV, the peak current is measured to be 3.3 kA/pulse with a 40 ns pulse width. A 10^{11} A/s rate for the current rise is obtained. A peak current high as 4.5 kA peak current is achieved when the 16 nF capacitor bank is charged with 40 kV. For each pulse, a charge of 0.4 mC is transferred by the mini-BLT.

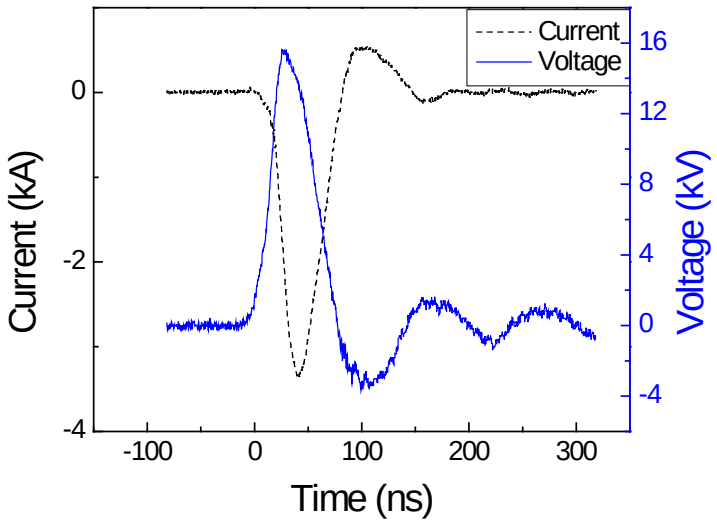

Figure 2.9 Voltage (solid line) and current (dashed line) waveforms recorded in the testing pulse forming network. Negative 27 kV charging voltage, 6 nF storage capacitance and 2.2 Ω load resistance are the parameters in this testing circuit.

The loop inductance is minimized with L = 80 nH. This inductance results

$$V_L = L\frac{dI}{dt} = 8kV \tag{2.7}$$

voltage loss in the loop. There fore the peak voltage measured on the resistor is at 16 kV.

The current density is around 10^7 A/m^2. And this is consistent with the current density prediction by thermionic enhanced field emission:

$$j_{TF}(T,E) = a(AT^2 + BE^{9/8})\exp[-(\frac{T^2}{C} + \frac{E^2}{D})^{-1/2}] \tag{2.8}$$

where T is the cathode temperature and E is the electric filed strength at the cathode surface. The parameters are

$$\begin{aligned} a &= 1.45 \\ A &= 120 \\ B &= 406E^{0.1(\varphi-4.5)}\exp[-2.22(\varphi-4.5)] \\ C &= 2.727\times10^9(\varphi/4.5)^2 \\ D &= 4.252\times10^{17}(\varphi/4.5)^3 \end{aligned} \tag{2.9}$$

In these equations, φ is the work function of the cathode in eV, T is in K, E in V/cm, j_{TF} in A/cm^2. If we plug in φ = 4.2 eV, T = 3200 K, E = 10^6 V/cm, then we can obtain j_{TF} at 10^7 A/m^2.

With high voltage and high power capabilities, the BLT is used in the pulsed generator to produce the transient plasma. A pulsed transient plasma ignition has been researched and

developed for pulse detonation engines with the promise of shorter ignition delay (with a factor of three or higher) and lean fuel ignition capability [Wang 2005b]. The non-equilibrium transient plasma was primarily comprised of streamers with high electric field head. This is the key to produce high energy electrons (10–15 eV) and increase radical generation by dissociating the fuel molecules throughout a large volume [Pancheshny 2000]. During the process of the transient plasma ignition, the high voltage pulse with a short duration time scale (less than 100ns) is essential to produce plasma streamers without arc formation, with a promise of shorter ignition delay, higher repetition rate and thus higher thrust.

By replacing the pseudospark switch with a mini-BLT in an in-house pulse generator [Wang 2005a] (the circuit diagram of the generator is shown in Figure 2.10a), the mini-BLT switches a 20 kV charging voltage and generates a 100 ns, 60 kV voltage pulse on a 100 Ω load. This pulse reliably produces transient plasma steamers in a 63.5 mm inner diameter combustion chamber, as shown in Figure 2.10b. Figure 2.10c is the voltage and current waveforms of this BLT switched pulse generator with a 100 ohm load resistor. The ringing at the tail of the pulse waveform is caused by the long grounding loop that is composed of the vacuum system and the pulse generator.

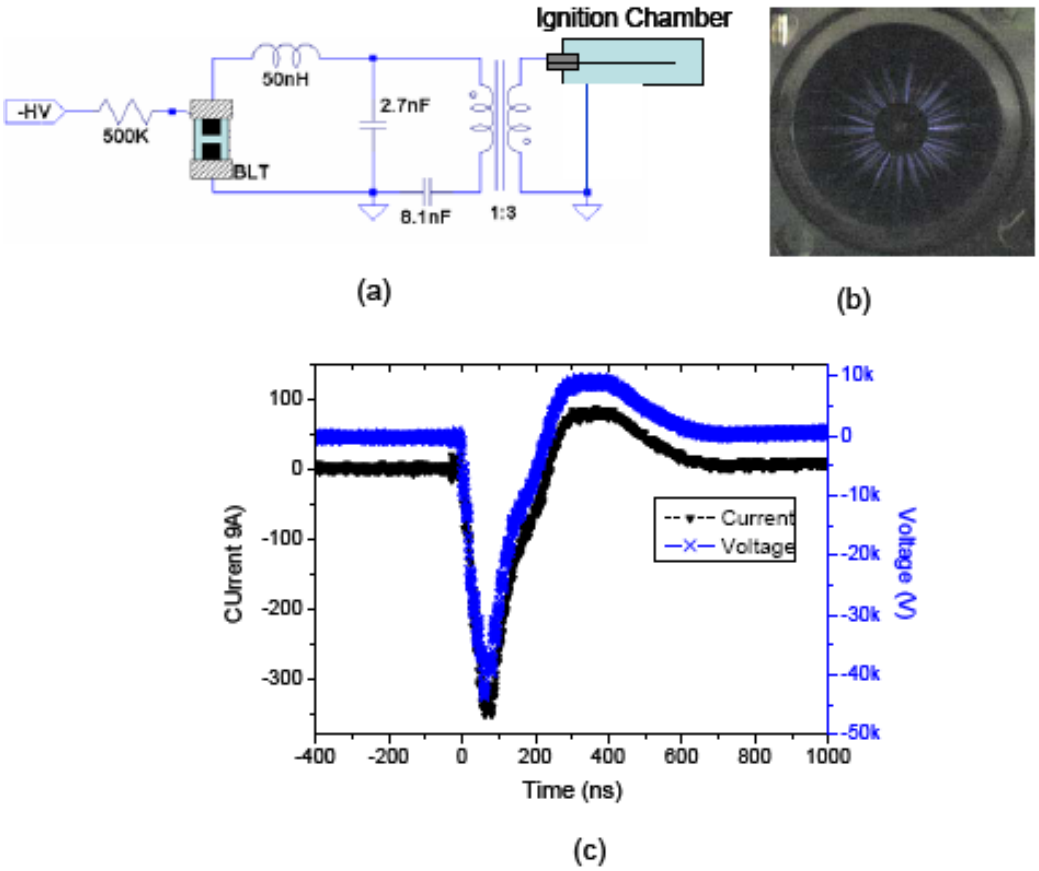

Figure 2.10 (a) Schematic of the transient plasma generator circuit. The BLT is used as the switch of the PFN, and the transformer ratio is 1:3. (b) BLT switched PFN generated streamers used for ignition of fuel air mixtures. Photo is taken by a CCD camera with 1 s exposure time. (c)The waveform of the current and voltage on the 100 ohm load resistor.

2.6 Chapter 2 future work

2.6.1 Brazed-BLT

The BLT switch prototype is directly connected to the vacuum system for experiments in a lab environment. However it is impractical to include a vacuum pump and gas tank for the real pulsed power applications. A sealed-off mini-BLT is under construction. In this case, it can be integrated to the real high power circuit. There are always trade-offs when one designs and determines the switch parameters. The testing with the mini-BLT prototype provided design reference for the sealed-off mini-BLTs. Figure 2.11 is the design schematic of the sealed-off BLT with the specific parameters of the switch dimensions. A ceramic housing with 2” length and 1” diameter is designed to be the insulator which contains the hydrogen getter and electrodes.

Ceramic to metal seals (or brazing) is chosen because it is a more robust and durable seal than glass seals. Properly designed ceramic to metal seals are able to maintain their hermeticity in a variety of harsh environments such as high and low (cryogenic) temperature, corrosive, high pressure, and high vacuum.

SAES Sintered Porous Getters (Parts No. : ST172/LHI/3-7/200) are selected to be the hydrogen reservoir—the gas container providing the hydrogen inside of the switch housing. Sintered porous getters are typically composed of zirconium powder mixed with other special powders and then sintered at high temperature under high vacuum. The

sintering process binds together all the zirconium particles resulting in getters with good mechanical strength and minimal release of loose particles. Although the getter has large surface area, it is small enough to be inserted into the cavity of the hollow electrode. Moreover, it has a self-integrated heater, therefore no heater circuit is needed to control the amount of gas released. Another advantage of the getter is its low activation temperature (400-500 ºC).

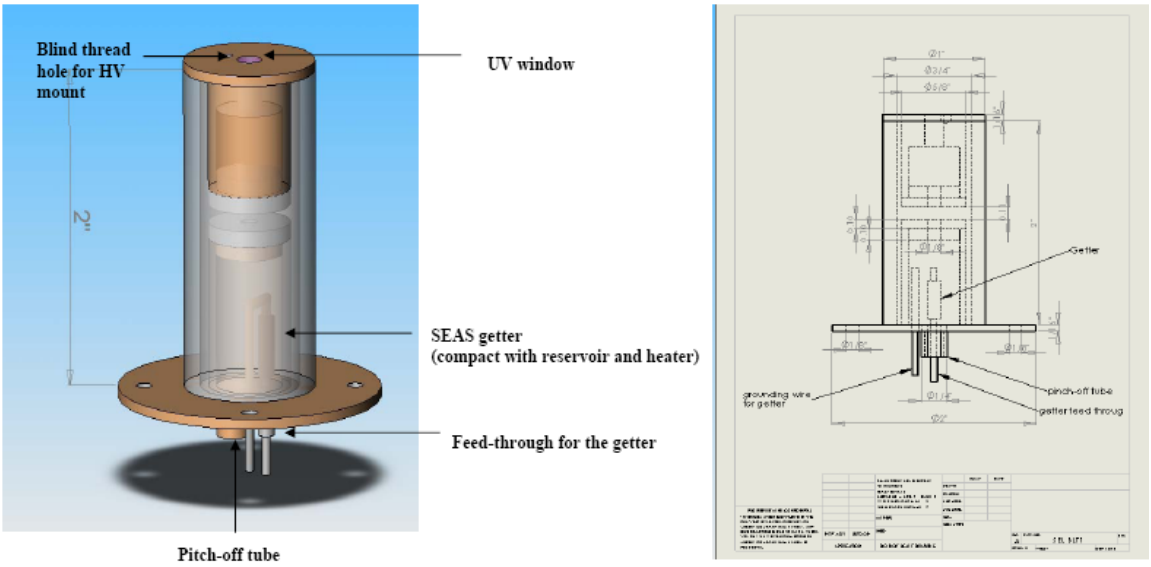

Figure 2.11 Design schematic of the brazed BLT with hydrogen getter integrated

There are several tips for using the getter:

1. The first activation should always be performed under pumping to allow most of the gases released in this step to be pumped away by the main pumping system.

2. Activation process for St 172: 450° C (or 3A current) for 10 minutes under a vacuum of greater than 10^{-3} Torr or an extremely pure rare gas atmosphere.

3. Need reactivation after exposure to air.

4. Do not allow the getter to touch other metal parts in the BLT.

5. Increase the current slowly for out-gassing the hydrogen to prevent an abrupt current rise from damaging the heater.

Mo, as in the prototype, has a high melting point (2623 °C) and UV triggerable work function (4.2 eV). Therefore it is remained the electrode material. When fabricating the electrode, the electrode surface needs to be polished to minimize the roughness and prevent early break-down. In addition, rounding the sharp edge of the aperture hole is also essential to avoid field emission from the edge. The electrode must be kept 1 mm - 1.5 mm away from the insulator wall to avoid surface flash-over between the high voltage and insulator. In order to avoid weak copper grips on the Mo electrode due to the

different thermal expansion, hydrogen-brazing the Mo to the copper with gold-copper-nickel solder is suggested.

Figure 2.12 shows the prototype of the CF vacuum flange sealed-off BLT. The getter and pinch-off tube are integrated at the grounding plate of the switch. UV window (a) or a fiber (b) (gas sealed by Epoxy patch sealant) is included to guide the light source. This BLT is installed in the circuit as shown in Figure 2.10a with 200 ohm load impedance. The voltage dropp on the load as well as on the BLT itself is measured (see Figure 2.12c).

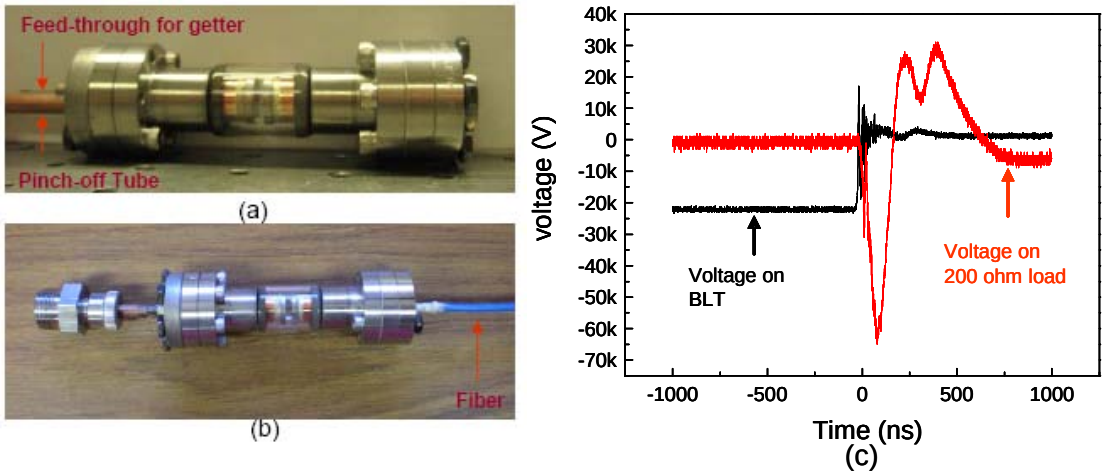

Figure 2.12 (a) CF vacuum flange sealed-off BLT with UV window and hydrogen getter. (b) Sealed-off BLT with fiber integration. (c) Voltage waveform on the BLT and 200 ohm load when circuit in Figure 2.10a is charged with 20 kV.

2.6.2 LED-trigger BLT

A laser triggered BLT has been tested and has the potential to be used in certain power level applications. However, the laser light source somehow limits BLTs' broad applications. On one hand, the volume of the laser system itself is comparatively huge and will increase the size of the overall switching system, on the other hand, the laser hugely increases the total price of the system. Therefore, cheap light sources as a replacement for the UV laser are under investigation. Nowadays, the wide-bandgap materials such as the III-V nitride semiconductors (GaN, AlGaN and AlN) make UV-LEDs and laser diodes possible. Doped aluminium nitride (AlN) has a very wide direct bandgap of 6 eV. And an AlN PIN (p-type/intrinsic/n-type) homojunction LED with an emission wavelength of 210 nm has also been developed. [Taniyasu 2006] A commercially available UV LED (UV-TOP 270, Sensor Electronic Technology, Inc) with a 270 nm emission wavelength is used for the primary test to explore the possibility of an LED trigger for the BLT.

The maximum DC current for UV-TOP 270 LED is 30 mA, however, the LED survives when it operates under pulse mode with much higher bypassing current. For primary testing, a TC4422 MOSFET driver is used to supply 120 mA pulsed current to the LED within 1 μs duration time (as shown in Figure 2.13a). The voltage drop on the LED is 11

V. The light emission from the LED is coupled to a UV fiber, and 0.3nJ/pulse optical pulse energy with 270 nm wavelength was measured after the fiber transmission.

Avalanche transistor based pulse generator is built to supply huge transient current to the LED. 550V DC voltage is held by the transistors and a current surge with 4 A peak current is released within 12 ns to the LED when the transistor is experiencing avalanche-breakdown. The circuit design of the avalanche transistor LED driver and driver current waveform is shown in Figure 2.14. The emission light was fiber coupled into the BLT with a coupling efficiency around 30%. Experimental results show that the current LED setup is not able to trigger the BLT.

According to references, 2 μJ in 300 ns pulse UV optical energy [Braun 1988] or 10^9 ~10^{10} electrons [Mehr 1995] is the critical number to ignite the proper BLT operations. If assuming the coupling efficiency is 100%, the quantum efficiency (QE) of the electrode materials is 10^{-5} and the LED optical energy is linearly proportional to the drive current (which is not actually true, because the emission light will get saturated when the current is high [Wang 2002]), the LED will output 25 nJ/pulse during 300 ns. This energy is still more than 100 times less than the critical ignition number.

There are several possible ways to improve the photoelectron yield. First, the optical output of the LED can be increased if an LED array is used, however the optical coupling

issue needs to be taken care of to ensure the high coupling efficiency. Second, LED with a shorter wavelength can produce more photoelectrons, but not orders of magnitude more. Third, new electrode materials with low work-function, high QE and high melting point may improve the photoelectron yield by orders of magnitude.

2.7 Chapter 2 summary

The design and operation of a small size version of the BLT (mini-BLT) are described in this chapter. Electrodes separation of 2 mm, cathode aperture diameter of 3 mm, cathode-thickness of 4 mm are determined as the electrode geometry specifications to optimized the hold-off voltages. This mini-BLT can switch high power pulses within 100 ns. Hold-off voltage up to 40 kV was achieved when the switch was filled with helium at 800 mTorr. The relatively high gas pressure results in faster switching speed and lower jitter and delay (30 ns ± 2 ns) than conventional pseudosparks. In addition, the small size of the switch and the short electrode separation (2mm) limit the inductance of the switch, which facilitates short pulse generation. A 4.5 kA peak current with a rate of current rise of 10^{11} A/s was observed. A laser trigger provides nanosecond delay time and jitter, while microsecond delay and jitter are obtained with a flash lamp trigger. The mini-BLT is able to transfer 120 MW peak power with 10 Hz repetition rate. The repetition rate is currently limited by the laser repetition rate, not by the switch itself.

The optical trigger minimizes the size of the switch, and reduces the switching delay and jitter. With total effective volume at about 15 cm^3, the mini-BLT is suitable for generating transient plasma streamers for ignition. A sealed brazed mini-BLT is under construction. This will be an advanced version of the current mini-BLT which will include the hydrogen reservior and maintain the vacuum by itself. It has the potential to replace the pseudospark in some high voltage pulse generators. At the same time, the mini-BLT largely helps to shrink the overall size and weight of the pulsed power system, which can promote the development of portable pulsed power.

The metal-ceramic brazed-off BLT is designed and under construction. The LED-triggered BLT is under investigation.

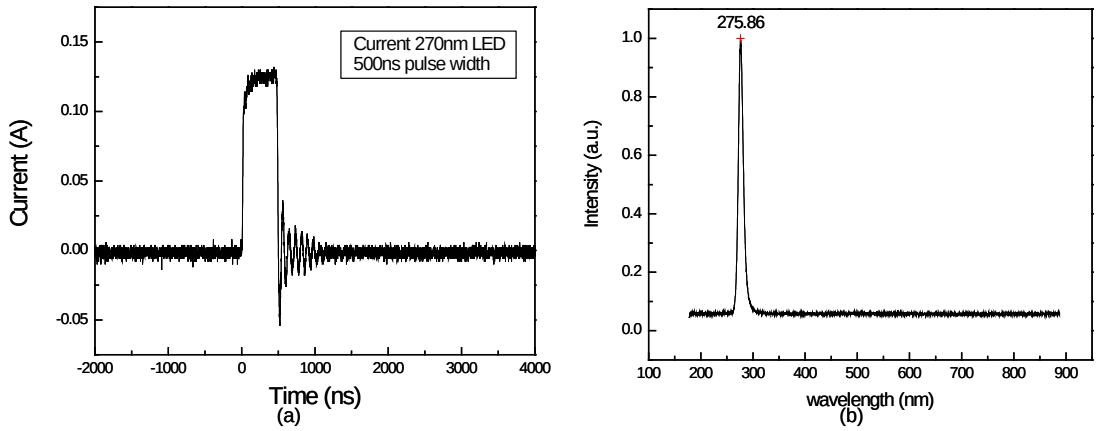

Figure 2.13 (a) Current waveform through the LED, generated from 4422 MOSFET driver. (b) Spectrum of the LED light emission.

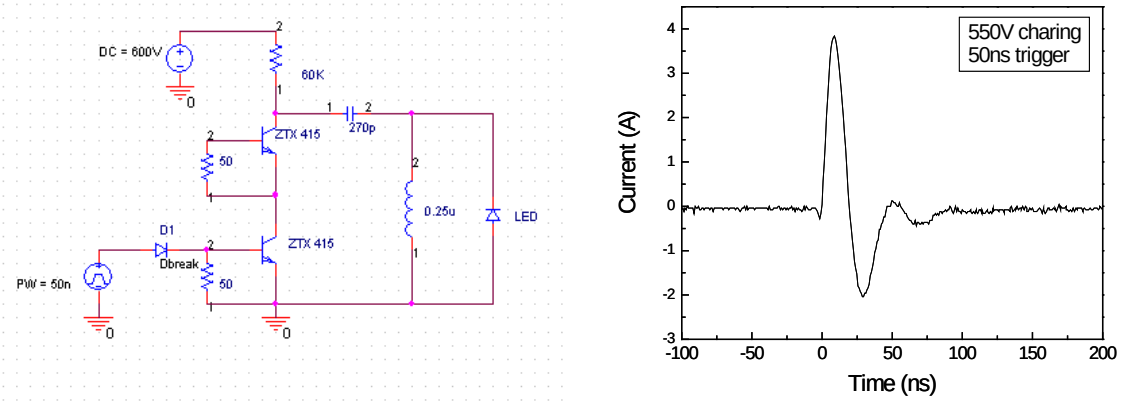

.

Figure 2.14 (a) Circuit diagram of avalanch transistor LED driver. (b) Current through the LED with 4 A peak current and 12 ns duration time.

Chapter 3: Dense Plasma Source for the Beam-Driven Plasma Wakefield Accelerator

This chapter will present a study of gas-filled hollow cathode cylindrical capillary discharge plasma sources. The capillaries have lengths between 4 and 20 mm, inner diameters between 0.3-3 mm and are filled with hydrogen at state pressures up to 1000 Torr. The plasma densities and temperatures as a function of the neutral gas pressure, the capillary length and the capillary diameter are analyzed by using Stark Broadening. And the longitudinal and time-dependent density profiles are also presented. Finally, the implications of the results regarding beam-driven plasma accelerators are discussed.

3.1 Capillary discharge

In some occasions the driver (either laser or electron beam) is intense enough to ionize a neutral gas and create the plasma, inside of which the wakefields are excited [Deng 2003]. In a similar way, a lithium vapor inside a heat-pipe oven [Vidal 1969] was used as a plasma source in the SLAC energy doubling PWFA experiment [Blumenfeld 2007].

Unlike in the Laser Wakefield Accelerator, gas jets and metal vapors, capillary discharge is a comparatively simple device that does not require an external strong driver to ionize a neutral gas.

Capillary plasmas are typically generated through the high voltage ionization in insulated tubes with internal diameters ranging from tens of micrometers to several millimeters. It is convenient to produce a pulsed discharge either by ionizing a gas that fills the capillary [Luther 2005, Ashkenazy1991] or by ablation of the capillary wall and electrodes [Rocca 1993b, Morgan 1994]. Capillary discharges were originally used in fusion research to obtain dense plasmas [Lochte-Holtgreven 1976], and more recently have been utilized in the development of x-ray lasers [Rocca 1993a, Rocca 1993b], EUV lithography [Kosner 1997] and the generation of plasma waveguides [Butler 2002, Gonsalves 2007] for the optical guiding of intense laser pulses.

Capillaries are great plasma sources for weak driving electron beams. In addition, the introduction of the extra parameters, such as the capillary diameter or the initial gas pressure, allows for better control of the selected plasma density.

3.2 Plasma spectroscopic diagnostics

3.2.1 Introduction to plasma diagnostics

Plasma diagnostics are methods used to measure properties of plasmas such as temperature and density. There are a number of techniques available for analyzing plasmas.

Measurements made with electric probes, called Langmuir probes [Langmuir 1924], are the oldest and most often used procedures for low-temperature plasmas. It works by inserting one or more electrodes into a plasma. The probe is surrounded by a plasma sheath and biased with a constant or time-varying electric potential. The measured currents and potentials in this system will determine the properties of the plasma [Cherrington 1982]. The diameter of the probe is typically required to be smaller than the Debye length. Thus this method is more suitably used in the low-temperature, low density plasma measurements when the probe size is practically constructed and shorter than the Debye length.

Optical methods are also common in plasma diagnostics. For example, Thomson Scattering is based on effects of the free charges on electromagnetic radiation [Fiocco 1963, Sheffield 1975]. The process of an electromagnetic wave being scattered by charged (elementary) particles may be thought of as follows: an incident electromagnetic wave affects the particle, and as a result of the electric and magnetic fields of the wave,

the particle is accelerated. The charged particle undergoing acceleration emits electromagnetic isotropic radiation. The diagnostic setup requires an external laser source that is focused into the plasma. The electromagnetic field of the laser will cause the plasma electrons to start oscillating and emitting radiation that is strong around the wavelength of the incident field. This radiation is much weaker than the incident radiation. The electron density can be determined from the intensity of the scattered light, but a powerful laser source and careful absolute calibration is required.

Laser interferometry is another plasma diagnostics method and it has recently been widely used in capillary discharge related experiments [Rowlands-Rees 2008, Spence 1999]. Plasma is placed in one arm of an interferometer. The plasma's index of refraction will depend on its density and will cause a phase shift in the incoming pulsed laser. The phase shift will be proportional to the plasma density integrated along the path. When a 2D spatial detector is used to record the interferometer signal, then information about the transverse profile of the plasma can be obtained, which is important for the intense laser waveguide [Gonsalves 2007]. The main drawback of interferometry is that the laser light may be deflected or absorbed by the plasma and distorts the interference signal, thus the density has to be extracted from the number of fringe shifts with extra care.

Other diagnostics such as laser induced fluorescence (LIF) [Davis 1983, Jacobs 2007], magnetic (B-Dot) Probe [Hutchinson 2002] and spectroscopy are also common for the plasma characterizations.

3.2.2 Stark broadening

Spectroscopic methods are accomplished by observing and analyzing the radiation spectrum of the emitted light. The principal diagnostic utilized in this thesis is Stark Broadening of hydrogen Balmer lines [Griem 1974], especially the H_α (656 nm) and H_β (486nm) lines. Even if the macroscopic electric field on the plasma is zero, any single ion will experience an electric field due to the neighboring charged particles in the plasma. The transitions of electrons between the perturbed atomic levels results in a broadening of some lines that can be used to determine the density of the plasma. In electrically neutral plasma, the perturbation filed strength produced by a particle located at on mean ion-ion distance is given by

$$E_0 = \frac{2.603 Z_p^{1/3} e N^{2/3}}{4\pi\varepsilon_0} V/m \qquad (3.1)$$

The field produces from ions that taken to cause virtually static Stark splitting of the energy levels is in the order of 10^8 V/m when electron density is 10^{19} cm^{-3}. In addition, the fast electrons are treated as projectiles and also produce a perturbation in the atomic

potential as they pass the atom. In a word, each Stark component can be considered collisionally broadened by the electrons and possessing a Lorentzian lineshape. The resultant is profile of the line intensity I(ω) at the frequency ω was found by Griem in Ref. [Griem, 1974].

$$I(\omega) = \frac{1}{\pi}\mathrm{Re}\left(\int dEW(E)d_{\alpha\beta}\right) \times \left\langle \alpha\beta \left| \left\{ j\omega - \frac{j[H_a(E) - H_b(E)]}{\hbar} - \phi_{ab} \right\} \right|^{-1} \alpha'\beta' \right\rangle d^*_{\alpha'\beta'} \tag{3.2}$$

Here, $H_a(E)$ and $H_b(E)$ are the Hamiltonians perturbed by the electric field E of the two atomic states a and b, and α and β are substates of levels a and b, respectively. Φ_{ab} is an operator that describes the electron's impact broadening. $d_{\alpha\beta}$ is the dipole moment operator.

In general, a larger plasma density will cause a larger Stark broadening. Stark broadening of the H_β line is considered to be accurate in identifying the plasma density only up to a density 3×10^{17} cm^{-3} [Ashkenazy 1991]. For diagnosing higher densities the H_α line must be analyzed. A sample hydrogen spectrum acquired during the work is shown in Figure 3.1.

When diagnosing the plasma, the plasma spectrum is first processed by subtracting the line background and finding out the FWHM linewidths $\Delta\lambda_{1/2}$ of the Balmer lines, which are measured by fitting the lines to theoretically-predicted Lorentzian shapes. Then, the

line intensity ratio between H_α and H_β lines or the intensity ratio between the background and emission line intensity can provide information on the plasma temperature [Griem 1974, Bekefi 1976], as

$$\frac{I(H_\alpha)}{I(H_\beta)} \propto \exp\left(\frac{E_\beta - E_\alpha}{KT}\right) \tag{3.3}$$

where I is the total emissive line intensity, E is the atomic energy level.

The intensity ratio diagnosis does not require the absolute intensity measurement which

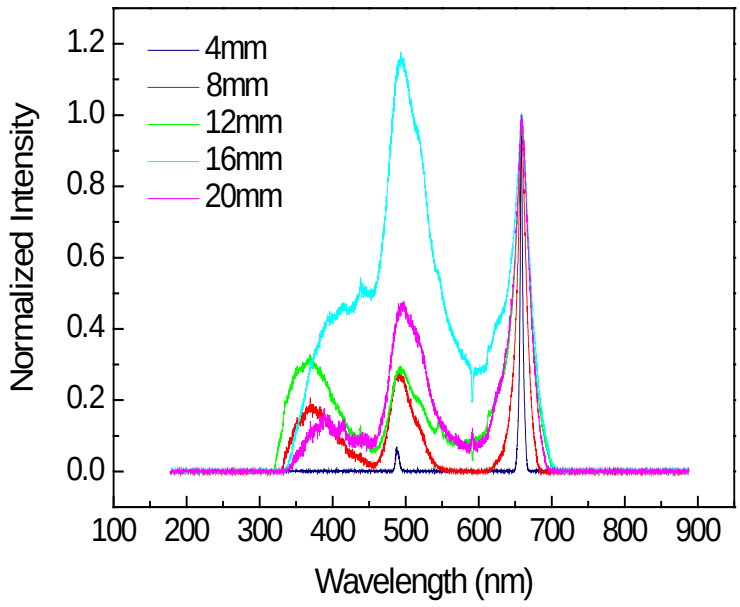

Figure 3.1 Hydrogen discharge spectra of capillaries with various lengths, and with a 140 Torr hydrogen fill. The diameter of all the capillaries is 0.6 mm and the applied voltage is 60 kV in all cases. The spectra are normalized to the peak amplitude of the Ha line. A discussion of the dependency of the plasma density as a function of capillary length visible is given below in section 3.5.4

minimizes the requirements for the equipment and setups. However it requires the Maxwellian velocity distribution in the plasma:

$$f_M = \left(\frac{m}{2\pi KT} \right)^{3/2} e^{-mv^2/2KT} \tag{3.4}$$

Also the plasma should be in local thermodynamic equilibrium (LTE) which requires sufficiently rapid process of the electron-atom and electron ion collision. For quickly check the satisfaction of the LTE, the particle densities should be larger than the criterion

$$N \geq 1.4 \times 10^{14} T^{1/2} \chi^3(m,n) cm^{-3} \tag{3.5}$$

where $\chi(m,n) = E_m - E_n$ is the energy difference between levels m and n. For the plasma with density of 10^{19} cm^{-3} in the capillary source, LTE is met properly.

Finally, the electron density n_e (in units of cm^{-3}) is calculated using the equation [Ashkenazy 1991]

$$n[cm^{-3}] = 8.02 \times 10^{12} \left(\frac{\Delta\lambda_{1/2}[\text{Å}]}{\alpha_{1/2}(n,T)} \right)^{3/2} \tag{3.6}$$

in which $\Delta\lambda_{1/2}$ is the Lorentzian-shaped hydrogen Balmer line width in Angstroms (after background subtraction), and $\alpha_{1/2}$ is a parameter weakly dependent on both the plasma density and the plasma temperature. The $\alpha_{1/2}$ coefficient can be obtained in the appendix table of Ref. [Griem 1974] for each spectral line.

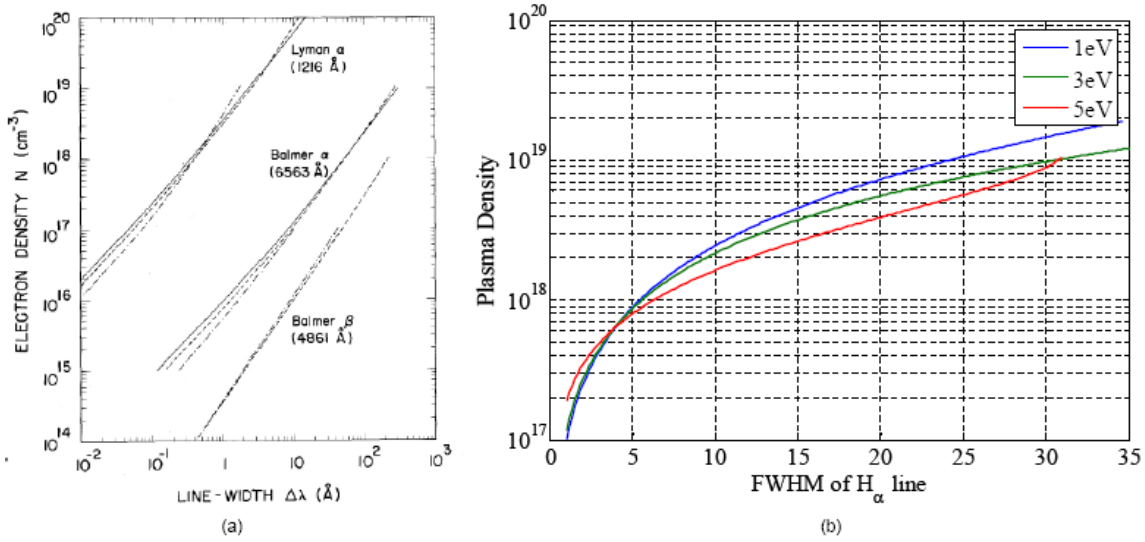

Figure 3.2 (a) FWHM as a function of electron density for different electron temperatures. (solid line-40,000K; dashed line-20,000K; dashed and dotted line-5,000K. [Bekefi 1976] (b) The H_a line as a function of FWHM based on equation 3.1.

Figure 3.2 shows the hydrogen Balmer lines' FWHM as a function of the electron density calculated using equation 3.1. For example, broadening of 30 nm of the H_α line is expected for a plasma density of 10^{19} cm^{-3}.

3.3 Experimental setup

3.3.1 Instrumentation setup

The experimental setup for the capillary plasma device is illustrated in Figure 3.3a. The capillaries consist of a 5 mm outside diameter borosilicate glass rod with on-axis

cylindrical holes of various diameters (0.3-3 mm). Each end of the capillaries with different lengths (4-20 mm) is attached to borosilicate glass tubes which work as the adapters for the o-ring sealed vacuum-ultra-Torr fittings, as shown in Figure 3.3b. This arrangement allows for variable pressure hydrogen gas fills within the capillary.

During the experiments, the valve between the capillary and the vacuum pump is closed, keeping the hydrogen pressure constant. Molybdenum hollow electrodes are fixed

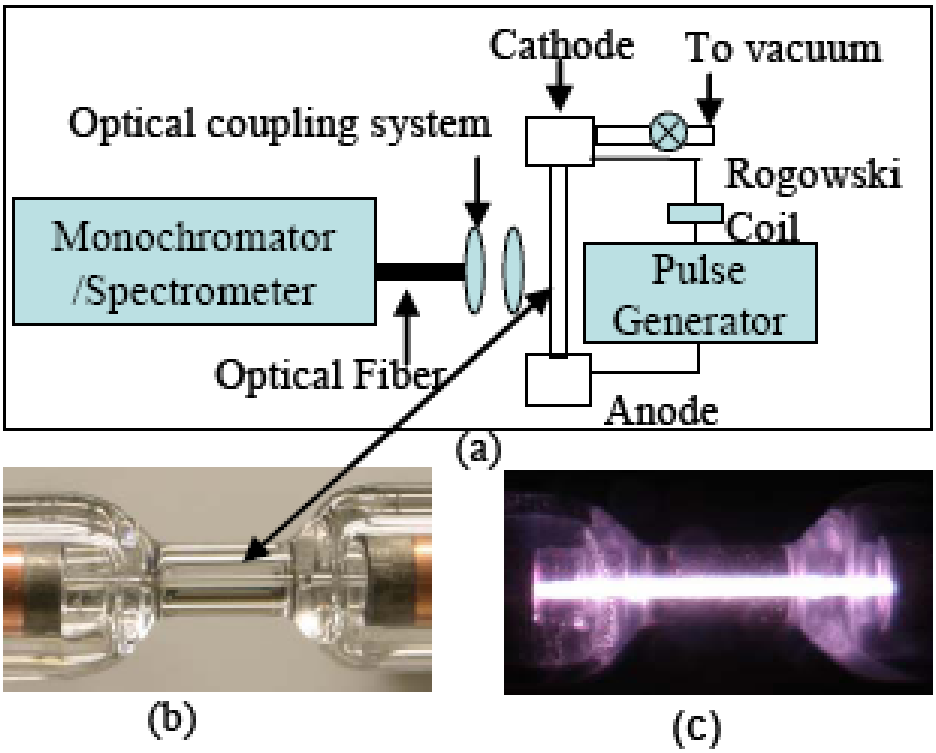

Figure 3.3 (a) Schematic of the plasma diagnostics system. The cathode is grounded. The PMT response time is 1 ns and it is mounted at the exit slit of the monochromator. (b) Photo of the 20 mm long, 0.6 mm diameter borosilicate capillary. Molybdenum electrodes with hollow cathode structure are used. (c) Discharge plasma in the capillary.

coaxially at the ends of the capillary (Figure 3.3b), delivering 60 kV peak voltage pulses from the in-house made pulse generator [Wang 2005b]. The discharge current is measured with a Rogowski coil. The light emitted by the discharge is collected and transported by an optical fiber to either a spectrometer or a monochrometer.

3.3.2 Time-resolved plasma density measurement

The time resolved plasma density is obtained by recording the amplitude of the light as a function of time for successive discharges with identical parameters while scanning the

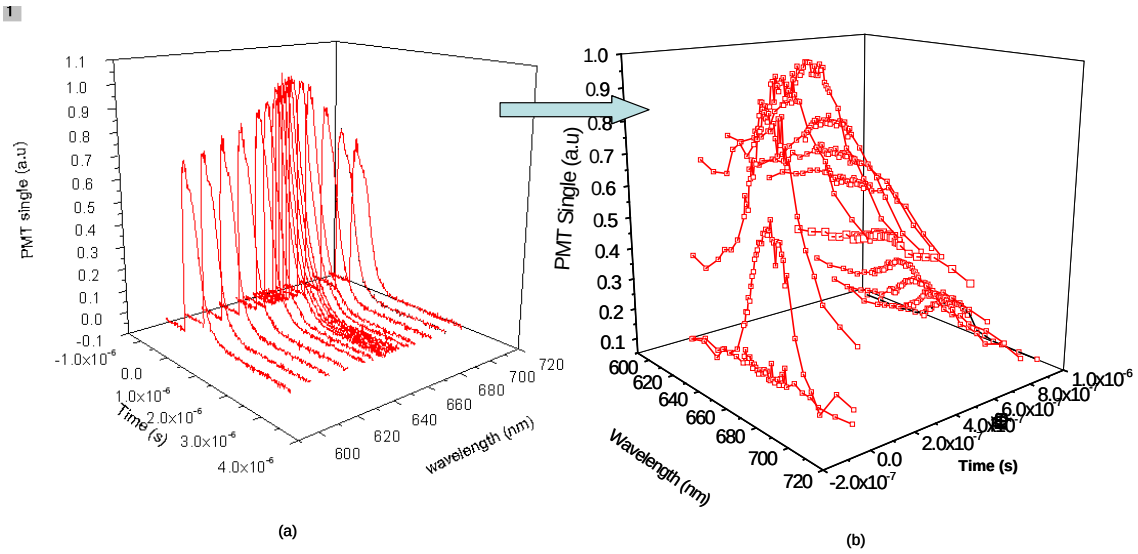

Figure 3.4 (a) A series of PMT signal after the monochrometer at different central wavelength. The unit of the intensity is arbitrary. (b) A series of time-resolved spectral line (600 nm – 900 nm) processed from data of (a).

central wavelength of the monochrometer from 600 nm to 700 nm with a 2 nm step size. A photomultiplier tube (PMT) with a 1 ns response time is mounted at the exit slit of the monochrometer, recording the light intensity as a function of time for each wavelength setting. Figure 3.4a shows a series of the PMT signal (light intensity as a function of time) obtained at different wavelength. The time-dependent spectrum is processed afterward by grouping the data from each wavelength for each point in time, as shown in Figure 3.4b. This procedure is appropriate because the discharge is found to have very small shot-to-shot variations. From the Lorentzian-shaped time-resolved H_α spectrum line, the plasma density information varies as time is retrieved.

3.3.3 Time-integrated plasma density measurement

In order to study the effects of the capillary geometry on the plasma density and temperature, an optical spectrometer is used with 1.6 nm resolution and 1 ms integration time. Since the integration time is longer than the discharge duration, it records the time integrated plasma light spectra. As in the previous experiments, the light is collected from the longitudinal center of the capillary. Figure 3.1 depicts plasma light spectra (normalized to the peak of the H_α line, λ = 656 nm) for different capillary lengths at a pressure of 140 Torr. The broadening of the Lorentzian-shaped H_α line indicates an increase in density, while the increase in H_β – to – H_α ratio (H_β at λ = 486 nm) indicates

an increase in temperature. The absorption line visible at 593 nm is attributed to Molybdenum ions originating from the ablation of the tips of the electrodes.

3.4 Time-resolved plasma diagnostics

3.4.1 Measurement results and discussion

By applying the methods described in 3.2.2, the time-resolved plasma density in a 12 mm long capillary with 0.6 mm inner diameter at a pressure of 434 Torr is presented in Figure 3.5, assuming a constant plasma temperature of 2 eV. The peak discharge current is 770 A with 150 ns duration. Around 400 mJ of electrical energy is delivered into the capillary for each shot. For the first 350 ns staring at t = 0, the pulse-induced noise disturbs the PMT signal and the density measurement. Between 350 ns and 1400 ns the traces show low noise and the measured density exhibits an exponential decay, $n_e(t)=n_{eo}\exp(-t/\tau)$, which can be fitted with a time constant τ = 300 ns. A density higher than 10^{19} cm^{-3} is achieved in the time interval between 400 ns to 500 ns and the peak density is $\approx 1.4 \times 10^{19}$ cm^{-3}. Beyond 1400 ns, the recorded signals are too weak to provide an accurate density measurement. Although the plasma temperature is assumed constant in this set of measurements, less than 5% variation in the value of the density is expected if the temperatures vary between 1 eV and 4 eV. Note that for these measurements, the light is

collected from a 5 mm-long section of the discharge, near its center. The signals are integrated over the discharge radius.

The diffusion constant in a cylindrical geometry can be estimated by assuming that the observed density decay is caused by the radial diffusion toward the capillary walls. Since the conducting plasma temperature is much higher than the wall temperature, the wall temperature is assumed zero [Bobrova 2001]. The mean electron lifetime is equal to $\tau_{diff}=\Lambda^2/D$, in which D is the diffusion coefficient and Λ is the cylinder characteristic diffusion length, which is defined by the formula [Raizer 1997]

$$1/\Lambda^2 = (2.4/R)^2 + (\pi/L)^2 \qquad (3.7)$$

in which R is the capillary radius and L is its length. Taking R = 0.03 cm and L = 12 mm, then $\Lambda^2 = 1.56\times10^{-4}$ cm^2.

Since the electron and ion densities are high, where $T_e \backsimeq T_{gas}$, then ambipolar diffusion is assumed as is the corresponding diffusion coefficient. Set D as the ambipolar diffusion coefficient:

$$D \cong 2D_i = 2\frac{2k_BT}{m_i\nu_m} \qquad (3.8)$$

in which D_i is the ion diffusion coefficient, k_B is the Boltzmann constant, m_i is the ion mass, υ_m is the effective collision frequency for moment transfer between electrons and atoms, and T_e is the electron temperature.

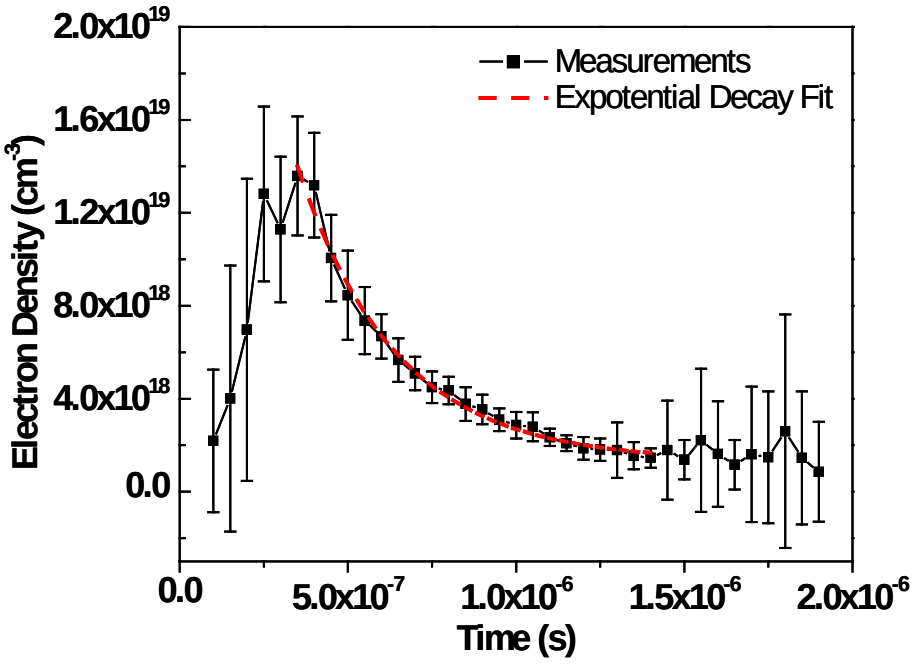

Figure 3.5 Time-resolved plasma density obtained in 12 mm long 0.6mm diameter capillary, and a 434 Torr hydrogen fill. The dashed red line is the exponential fit to the part of the curve with good signal to noise ratio: 400 ns<t<1.4 μs. Before t=400 ns discharge noise dominates the PMT signal. After t=1.5 μs the light signal is too weak. The applied voltage is 60 kV.

For ionized plasma, the effective collision frequency for moment transfer:

$$\nu_m = Nv\sigma_{tr} \tag{3.9}$$

in which σ_{tr} is the momentum transfer cross section (the typical value is 10^{-15} cm^{-2} t), and

$$v = \left(\frac{2k_B T}{m_i} \right)^{1/2} = 1 \times 10^6 cm/s \tag{3.10}$$

Then we can finally derive D=383 cm^2/s, and then τ_{diff} = 4 × 10^{-7} s. The calculated lifetime is close to the experimental measurement of Figure3.5 (300 ns). In this calculation, the density of electrons is assumed constant at N = 5×10^{18} cm^{-3}.

Since the discharges lasts for several μs, the injected relativistic beams travel close to the speed of light, a beam will transverse the capillary length in a matter of ps, which is much shorter than the plasma density decay time. The plasma density therefore is considered on constant fro the PWFA process. The proper timing between a beam and the discharge allows for a plasma density in the order of $10^{14} – 10^{19}$ cm^{-3}.

3.4.2 Optical study for the plasma channel formation

In addition to the spectral measurements presented in the previous paragraph, the process of the formation and decay of the plasma channel is studied by using a fast gated camera (with 4 ns gating time) to capture the pseudo-color discharge images that are shown in

Figure 3.6a. For these images, the capillary is 12 mm long, and 0.6 mm in diameter. The images show that during the first 40 ns, the gas forms a weakly ionized channel, initiating from both electrode ends and expanding into the middle of the capillary simultaneously. Subsequently, the plasma expands into the entire capillary and the peak light intensity is reached around 200 ns after the initiation of the discharge. Finally, the intensity diminishes gradually soon after that peak is reached. The intensity drop is sharper near the electrodes, which indicates faster recombination near the boundaries. By integrating the overall intensity of each time-resolved images shown in Figure 3.6a, the light intensity signal versus time is fitted with an exponential decay as well, as shown in Figure 3.6b. And the derived time constant is around 500 ns, which is in the same order of the magnitude as the time constant obtained from Figure 3.5.

3.5 Time-integrated plasma diagnostics

The time-integrated capillary plasma diagnostics can provide information about the dependence of the plasma density and temperature on the various factors controlling the parameters. These factors are important because they allow design flexibility when a certain plasma source is to be designed for a plasma wakefield experiments or other applications. The experimental setup is shown in section 3.2.3. Every possible measure was taken so that only one parameter was varied at any given time, with everything else

remaining constant. Unless otherwise noted, the charging voltage was set at 60 kV and the peak discharge current is measured to be around 750 A. Fluctuations of few tens of amps are observed for the different capillary lengths and gas pressures.

According to reference [Granovsky 1971, Kallos 2005], the temperature difference between the electrons and the heavy particles (ions and gas molecules) is small when $n_e > 10^{16}$ cm^{-3}. Since the capillary plasmas satisfy the above density condition for most of the time (refer to Figure 3.5), the dense equilibrium low-temperature plasma theory is applied to explain the dependence of the plasma density on the capillary geometry in the following two sections. In this theory, “The field pumps energy into the electron gas as a whole. Electrons are thermalized through collisions with one another and through subsequent maxwellization of their distribution.” [Raizer 1997] The gas is finally ionized by the secondary electrons that obtain energy from the collision exchanges, and not from the field.

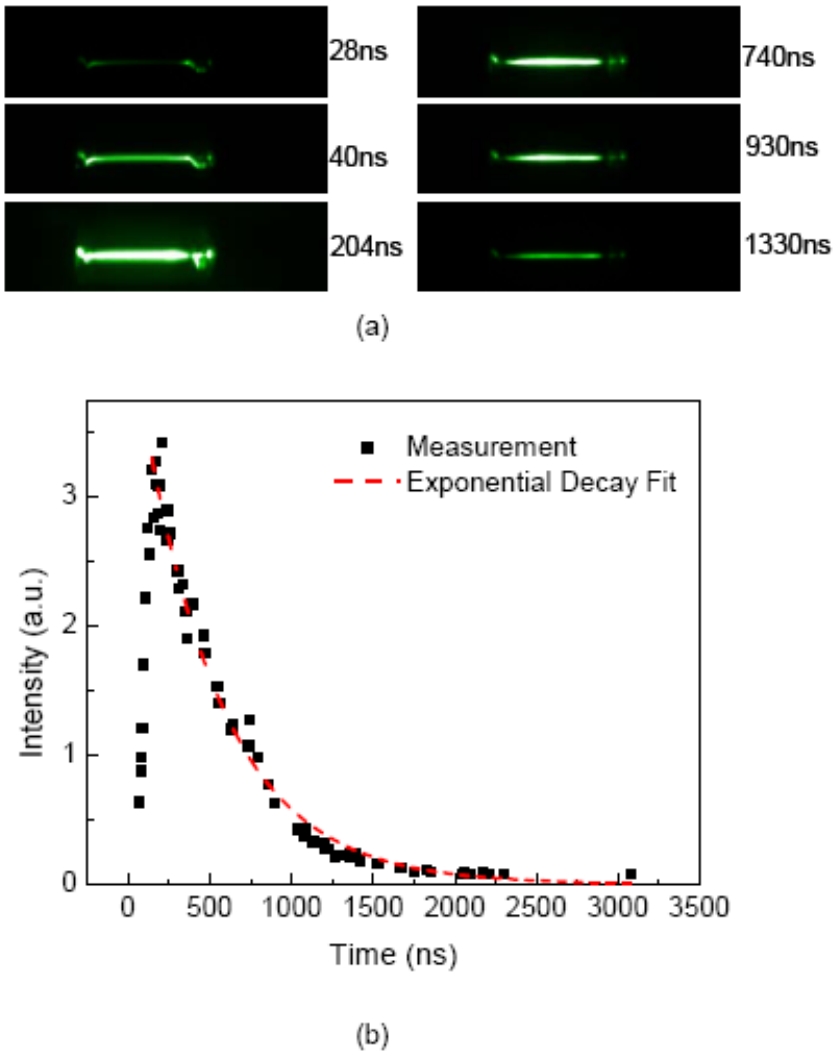

Figure 3.6 (a) Images of the plasma captured by a LaVision PicoStar ultra-fast camera with 4 ns gating time. A neutral density filter is applied to avoid saturation. The green color is the pseudo-color of the camera. The color scale of the images is chosen to show all the weak discharges above. No wavelength selection is performed. Reflection and refraction distort the discharge images at the junctions between the capillary and glass tube. (b) The discharge intensity varies as a function of the time. The red dashed line is the exponential fit for the decay of the intensities.

3.5.1 Life-time of the capillary

The clean H_β and H_α spectral lines in Figure 3.1 indicate that the wall ablation of the capillaries is weak. This is consistent with the fact that in these setups the temperature near the wall is lower than the temperature near the axis, where the electrons impact the wall with low energy and cause minor wall sputtering. The gas-filled capillary remains robust after 10^3 shots, thus providing a much longer lifetime than the ablative capillaries.

3.5.2 Plasma density dependence on capillary radius

The plasma density has a strong dependence on the capillary radius. Higher plasma densities are experimentally obtained at all pressures with the smaller diameter capillaries, as seen in Figure 3.7. Since the plasma temperature is highest on the capillary axis while at the capillary wall the plasma remains close to room temperature, there is a large temperature gradient across the radius of the plasma. The heat flows from the axis to the wall and satisfies the energy balance equation (or Elenbaas-Heller equation):

$$\frac{1}{r}\frac{d}{dr}(r\kappa\frac{dT}{dr})+\sigma E^2=0 \qquad (3.11)$$

in which κ is the thermal conductivity, r is the capillary radius, T is the radius-dependent plasma temperature, E is the electric field, σ is the electric conductivity, and σE^2 is the ohmic heat source term. Assuming the axis temperature remains the same when the capillary radius is reduced, the temperature gradient increases. As a result, the heat

diffusion (the first term on the left hand side of equation 3.2) increases. In order to sustain a steady energy balance, more energy is injected into the capillary, which eventually increases the gas temperature and causes more ionizations according to the Saha equation:

$$n_e \propto \exp(-I/k_B T_{gas}) \tag{3.12}$$

in which I is the ionization potential and T_{gas} is the gas temperature. Although higher plasma densities are obtained in a smaller diameter capillary, our main interest for these

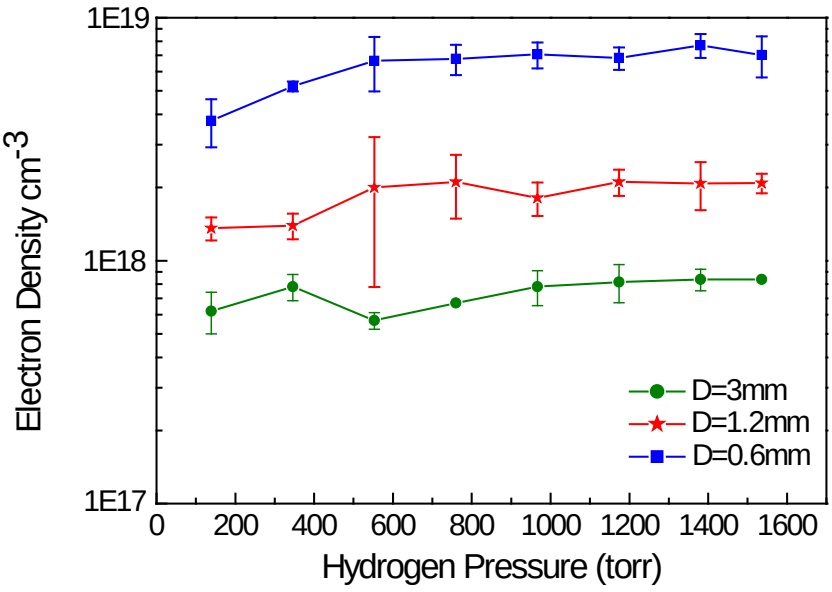

Figure 3.7 The dependence of the plasma density as a function of pressure for 3 different capillary tube diameters. The capillaries lengths is 20 mm and the discharging voltage is 60 kV.

studies is in the capillaries with 0.6 mm diameters since they provide a specific desired density ($>10^{19}$ cm^{-3}) while at the same time allow electron beams with transverse spot size as large as σ_r = 100 μm (typical size for low energy electron beams) to cleanly pass through the capillary.

3.5.3 Plasma density dependence on gas pressure

When the pressure increases the measured plasma density is observed to increase (see Figure 3.8). Since radiative heat cannot be ignored at high pressure, the radiative loss term is included as an additional term on the left hand side of equation 3.2. When the pressure increases, more heat is lost through radiation and more energy is forced to be delivered into the gas to meet the energy balance, and therefore more ionization takes place. However, the three-body recombination rate, which decreases the density, is also enhanced at higher gas pressures, limiting the degree of gas ionization. As a result, the plasma density increases with pressure at a less than linear rate on seen on Fig 3.8.

3.5.4 Plasma density dependence on capillary length

In most gas-filled capillary simulations, aimed mainly towards laser-driven accelerator applications [Bobrova 2001, Broks 2005], the effect of the capillary length is omitted because one-dimensional radial models are used. However we have observed that the

capillary length influences the plasma density (see Figure 3.9). In order to investigate the dependence of the plasma density on the capillary length, we derive the radially-averaged temperatures from the H_a line to background intensity ratio, which we subsequently use to calculate the plasma density. Figure 3.9 illustrates the dependence of the time-averaged plasma density and temperature on the capillary length as deduced from spectra similar to those in Figure 3.1.

We observe that when the capillary length increases from 4 mm to 12 mm, the electron density increases as well. We believe that this happens because the ohmic resistance of the plasma increases with longer capillary lengths, which results in a more optimal impedance matching of the plasma to the pulse forming network (PFN), and therefore to a larger, more efficient energy transfer from the PFN to the plasma through a greater ohmic heating. When the length of the capillary is increased further beyond 12 mm, the density decreases. The physical inside of this dependence of plasma density on capillary length has not been well understood yet. However, this is probably related to the decrease of the electric field (applied voltage kept constant to 60 kV). As a result, the number of the “seed” electrons, which are initially produced by the electric field and cause secondary ionization later, are reduced. Moreover, when capillary length increases, the electrical filed decreases. The recombination and diffusion loss of the electrons compensates the secondary ionizations. When the electrical field is less than a critical

value, a self-sustaining current can not be maintained and discharge channel fails to form. In addition, a maximum in the hydrogen total scattering cross section has been previously observed when the plasma temperature is around 3 eV [Raju 2006]. With a high cross section, the energy exchanges are enhanced. The trade-off between the generation of the "seed electrons" (depends on the electrical field) and the variation of the overall energy delivered from the PFN may lead to an "optimum length" of 12 mm with the largest plasma density (see Figure 3.1 and 3.9b). Finally, for capillary lengths beyond 30 mm, breakdown is not achieved when the gas pressure is 760 Torr or higher due to Paschen law limitations.

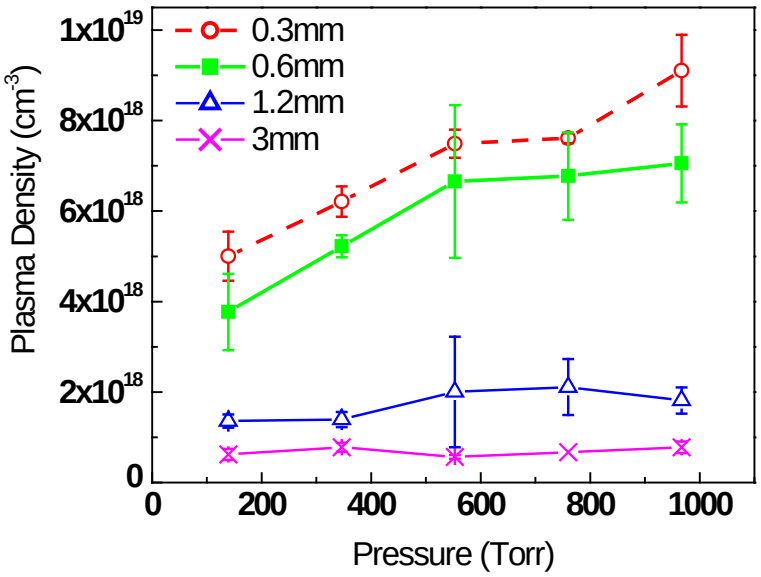

Figure 3.8 Time integrated plasma density as a function of the fill pressure for various capillary diameters. All the capillaries have a fixed length of 20 mm (solid lines) except the one with 0.3 mm diameter (dotted line) which is 16 mm long. The applied voltage is 60 kV

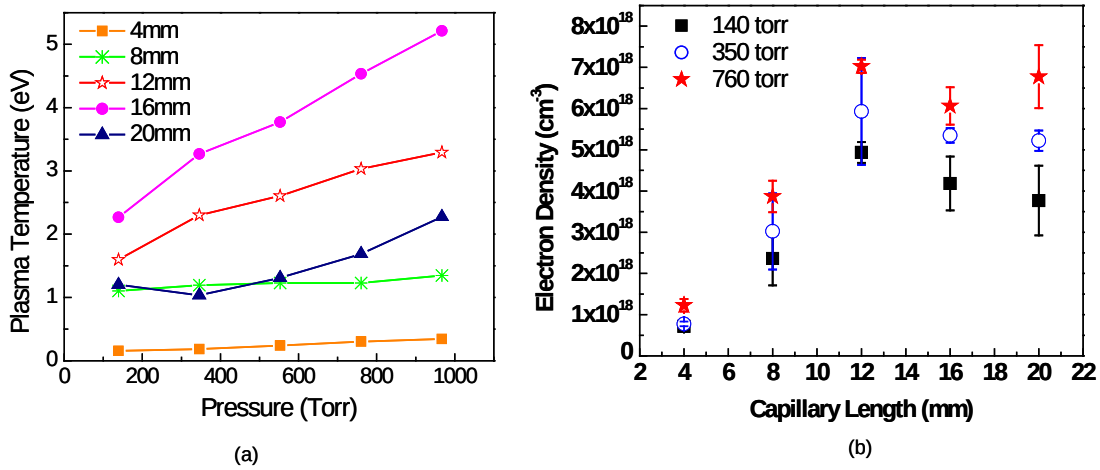

Figure 3.9 (a) Plasma temperature and (b) plasma density with capillaries with various lengths as a function of hydrogen pressure. All of the capillaries have a diameter of 0.6 mm, and the applied voltage is 60 kV.

3.5.5 Plasma density dependence on electrodes structure

Hollow electrodes are used to deliver the high voltage pulse, although no significant effect on the plasma density is observed when they are replaced with the flat, solid ones. The micro-hollow cathode scaling law requires the product of neutral gas pressure p times the electrode hole diameter D, p·D, to be in the range of 0.1-10 Torr·cm in order to establish a super emissive mode. This condition is not satisfied for the high densities of interest here. As a result, no significant density difference is observed with the two electrodes are presented, as shown in Figure 3.10. However electrode-specific erosion is argued to be 2 – 3 orders of magnitude lower with the hollow cathode electrodes [Raizer 1997]. We therefore used hollow electrodes for all the experiments. Moreover, for PWFA applications, the holes are necessary for the passage of the e-beam through the capillary and plasma.

3.5.6 Longitudinal plasma density distribution

The longitudinal time-averaged distribution of the plasma density along the capillary length was also measured. The plasma density remains within a 10% range over a 6 mm length near the center of the 12 mm long capillary, and it drops by nearly a factor of two when close to the cathode (see Figure 3.11). This distribution is also observed in

capillaries for LWFA applications, and causes problems with the external injection of electrons into the driven wakefields [Levin 2005].

For resonant or multi-bunch PWFA applications [Kallos 2005, Kallos 2008b], the density must be as uniform as possible over a long enough length, such that a large wakefield amplitude can be driven over a distance comparable to the capillary length and energy gain can be observed. The plasma and the bunch train driving the wakefield will only be in resonance along the length over which the plasma density variation is within approximately 1/N, in which N is the number of bunches in the drive train. The longitudinal density measurement shows that a variation of <20% is measured over ≈8 mm of plasma, which is appropriate for experiments planned with N=5 bunches.

3.6 Chapter 3 future work

After the development of the high density plasma source, the most feasible testing would be the acceleration of trailing witness bunches using this source. It is extremely important to demonstrate in an experiment that multiple drive bunches can provide wakes with a high energy transformer ratio. ATF could provide the first proof-of-principle results at low energies, but eventually these schemes need to be tested in GeV-scale machines.

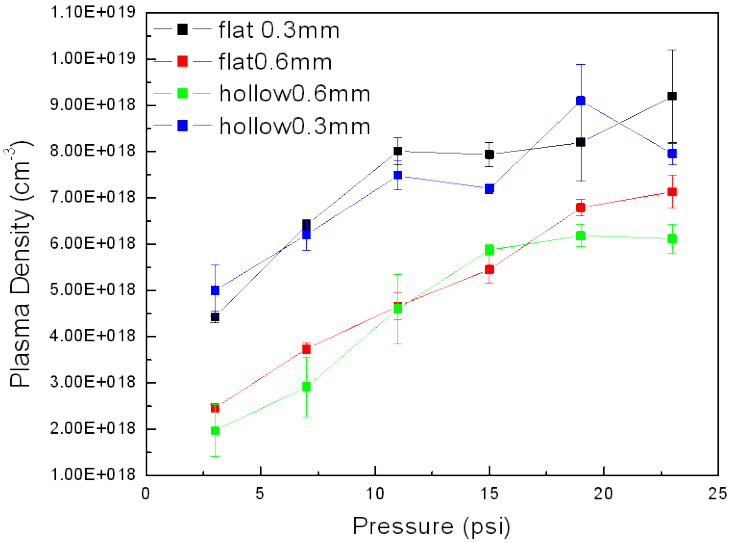

Figure 3.10 Plasma density in a 16 mm capillary as a function of pressure for two different capillary diameters. Two different types of electrodes (flat and hollow) were also tested.

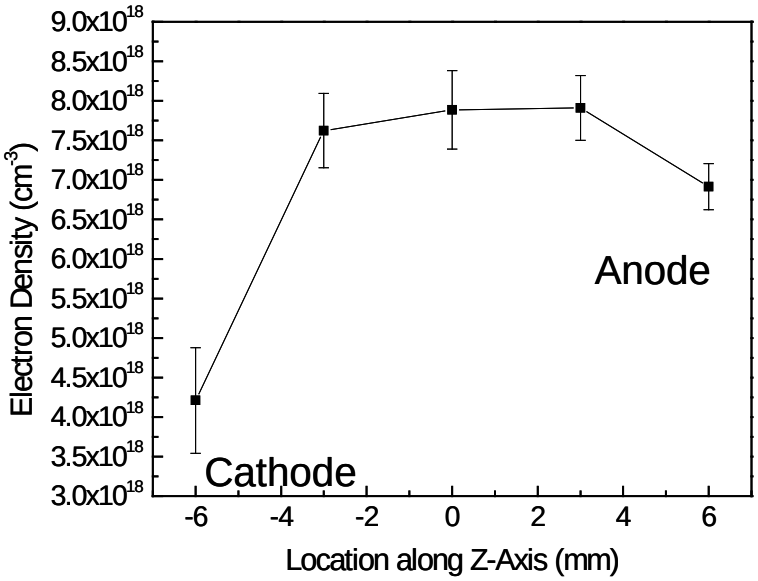

Figure 3.11 Plasma density along the capillary axis for a 60 kV discharge in a 17 mm long capillary at 1 atm of pressure. The error bars indicate density variations over 10 discharges

In addition to the acceleration application, the capillary plasma source can be used for lighting applications. During the experiment, high intensity light emission is observed from the gas discharge inside of the capillary. The wavelength of the light is determined by the gas in the discharged. Xenon vacuum ultraviolet (VUV) emission at 172 nm as obtained in a 180 μm diameter capillary [Lee 2007]; and as short as 46.9 nm soft-X-Ray is obtained through Ar discharging in a 12 cm long capillary [Rocca 1994]. Except for the UV and soft-X-Ray emission (which could be used for bacterial sterilization, photo lithography and X-Ray laser development), the visible range emission from hydrogen, nitrogen or helium might play a role in exciting fluorescence in particular dyes to assist the biological observation.

From the preliminary experiment result, there is a broad band spectrum in visible range with high intensity when hydrogen discharges in the 0.3 mm inner diameter capillary, as shown in Figure 3.12a. Therefore, a high-intensity lamp is proposed to be built, based on the capillary discharge. The Figure 3.12b shows a linear relationship between the light intensity and the gas pressure. Stronger intensity can be achieved with higher gas pressure in the capillary.

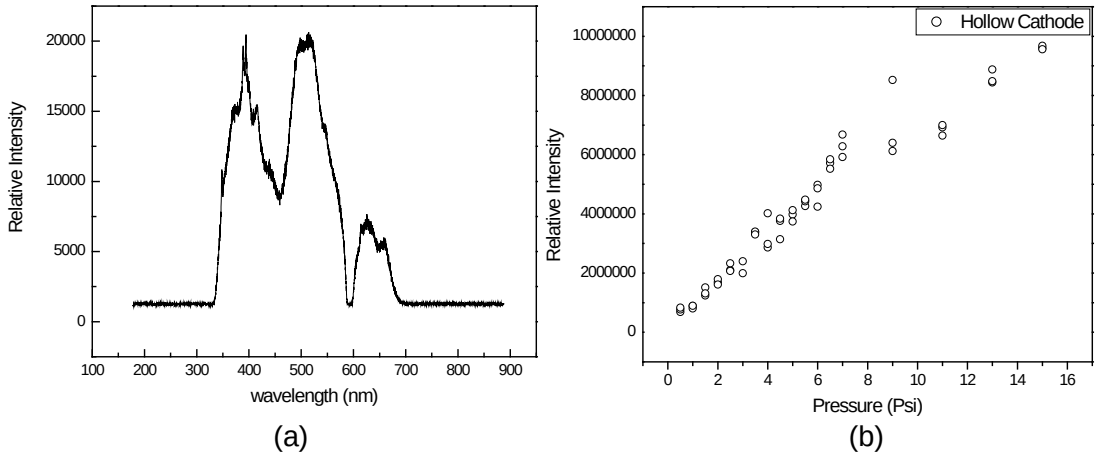

Figure 3.12 (a) Hydrogen spectrum when discharged in 0.3mm inner diameter capillary. (b)Relative total discharge intensity varies with the hydrogen pressure.

3.7 Chapter 3 summary

In summary, we have developed a low cost, relatively simple and effective high-density hydrogen plasma device. High density discharges in 0.6mm diameter capillaries with lengths up to 20 mm are obtained with pulsed voltage of 60 kV. This hydrogen-filled capillary plasma source is able to produce plasmas with controllable densities ranging from 10^{16} cm^{-3} up to 1.4×10^{19} cm^{-3} by changing the gas pressures. Time-resolved measurements indicate that a density higher than 10^{19} cm^{-3} is achieved in a time interval between 400 ns to 500 ns. For multi-bunch PWFA applications, the plasma density that leads to resonant excitation of the wakefield can be selected by choosing the time delay

between the discharge and the electron beam arrival time in the plasma. The beam must travel in the plasma after the discharge current has disappeared to avoid possible strong beam deflection due to the plasma current and magnetic field. Although the hydrogen gas is not fully ionized, further ionization by the multi-MeV electron beam is not expected to contribute to the plasma density due to the low cross section for impact ionization. The device is pulse-repeatable with a long lifetime. After 10^3 shots, no sign of damage is observed. We plan on using this device for multi-bunch PWFA experiments in the 10^{16}-10^{19} cm^{-3} regimes.

The application of the fluorescence excitation source and lighting source using the light emission from the capillary are also proposed.

Chapter 4: Solid State Switched Pulsed Power Circuit Design

In Chapter 2, gas type switches, especially the Back-Lighted Thyratron, are introduced. They benefit from high power handling capability and fast switching ability. However, the gas type switches normally need the vacuum brazing technique to maintain the low pressure, and that increases their size and cost. On the other hand, high voltage semiconductor solid-state switches, such as power MOSFETs, IGBTs, SCRs, thyristors, etc. can be small and inexpensive, but are rated for less than 10 kV. The current rise-time is also an issue for high current, short pulse operations. If we use a semiconductor switch with high-speed but small capacitance, we must use a switching valve that includes many parallel and series connections. Solid state switch arrays are typically used for high power applications.

This chapter will introduce several pulsed power topologies that are realized by using only solid state components. We focus on the Marx Bank, magnetic pulse width compression, and diode opening.

4.1 Marx Bank generator for skin cancer therapy

4.1.1 Basic operation principle

A Marx Generator was originally described by Erwin Otto Marx in 1924. Marx generators are implemented as a way of charging a number of capacitors in parallel, then discharging them in series, ideally producing an output voltage equal to the input voltage multiplied by the number of capacitors.

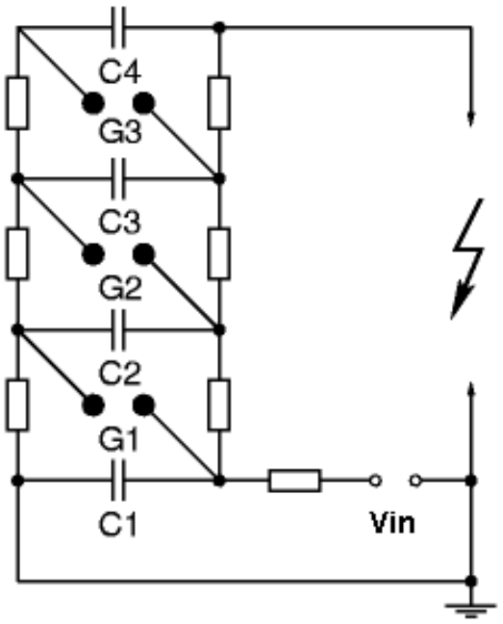

Figure 4.1 Schematic of a Marx Bank generator.
(www-project.slac.stanford.edu/ ilc/meetings/thursday/ILCMarx24Mar05.ppt)

Figure 4.1 shows the schematic of the general structure of the Marx Bank. During the charging state, switches G1, G2, and G3 are open, capacitors C1, C2, C3 and C4 are in parallel and charged with voltage Vin. Each capacitor holds the voltage of Vin. When G1, G2 and G3 are switching on simultaneously, the capacitors discharge in series. Since the capacitor appears the resistance for the voltage variation, the potential difference will be held by each capacitor temporarily. Thus the voltage on each capacitor will be added up and the final output voltage has the value of the number of the capacitors times the charging voltage. One of the most important issues in the Marx generator is the floating ground problem for the switches. The switch electrodes experience high absolute voltage potentials when they are conducting between the capacitors.

4.1.2 Self-triggered Marx Bank

An optical isolator or transformer can solve the switch floating problems by generating the potential difference for switch triggering, thus, no grounding is needed for solid state switches. Instead of the usage of isolators, a self-triggered MOSFET switched Marx Bank [Baker 1993] is built for bio-medial applications. Figure 4.2 shows the circuit diagram of this Marx Bank. A bipolar transistor is used as a MOSFET driver to supply gate current to M1. Once M1 switches on, the source voltage of M2 becomes –V2, the source voltage of M3 is -2×V2, and so on down the line. In order to avoid the MOSFET damage, the

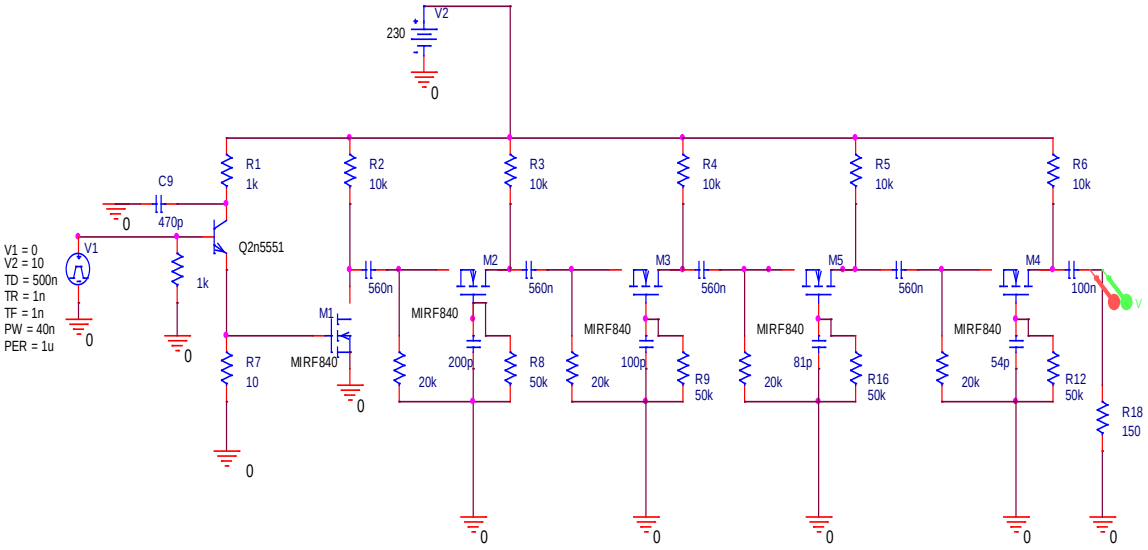

Figure 4.2 Marx Bank generator circuit diagram

gate-source potential difference on each MOSFET should be less than 20V. Therefore, capacitor C_g in series with the MOSFET gate-source effective capacitor C_{gseff} works as a capacitive voltage divider to satisfy the requirement which is given by

$$\Delta V_{gs} = 20 = \Delta V_{sN} \cdot \frac{C_{gN}}{C_{gN} + C_{gseff}} \tag{4.1}$$

Where ΔV_{sN} is the source voltage on Nth MOSFET, therefore, ΔV_{sN} = -(N-1)V2.

So

$$C_{g2} = \frac{20 C_{gseff}}{\Delta V_{s2} - 20} \tag{4.2}$$

And

$$C_{gN} \approx \frac{1}{N-1} C_{g2} \tag{4.3}$$

Since the gate capacitance of power MOSFET IRF840 (Vds = 500V, Vgs = 20V, Ids = 8A, 32A for pulse mode, turn on time = 21ns) is around 3000 pF, the capacitance in series with the MOSFET (M2, M3, M4, M5) gate are 200 pF, 100 pF, 81pF and 54 pF respectively. The final output voltage is determined by the charging voltage times the stage number, and the voltage pulse width is determined by the MOSFET on-time, which is related to the triggering duration time at the first stage of the Marx Bank.

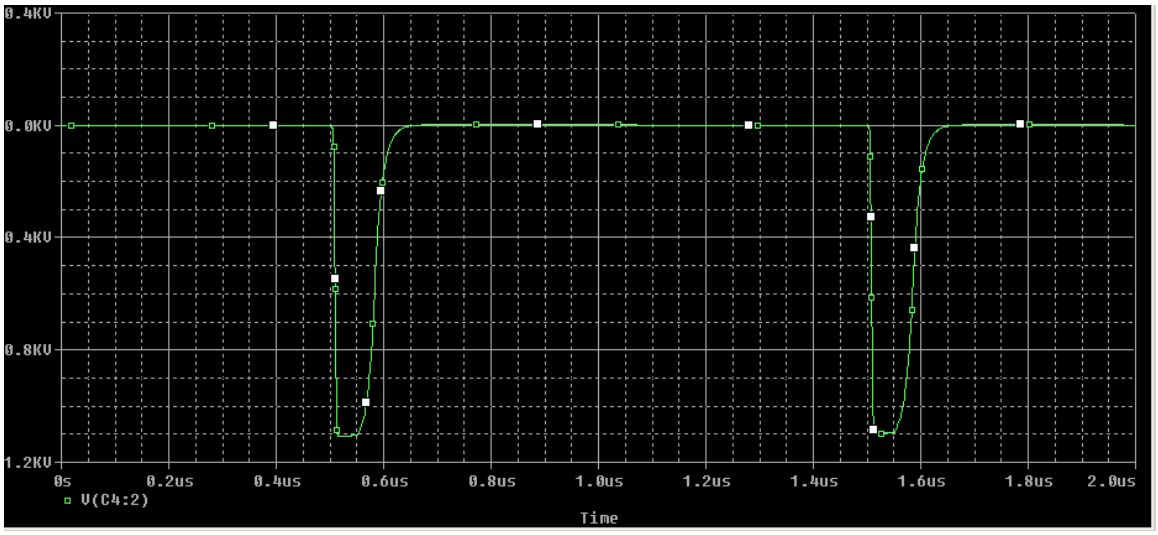

Figure 4.3 Spice simulation result. Charging voltage V2 is 230V, trigger for MOSFET driving is 10V, 40ns at 100 Hz, the load 150 ohm. The output voltage is 1.1 kV, pulse width is 100 ns with repetition rate of 100 Hz.

Figure 4.3 shows the SPICE simulation result of the circuit. A 150 ohm load, which is the equivalent impedance of the micro-chamber [Sun 2005], is included at the output of the generator for Spice simulation. With 230V charging voltage on the coupling 560 nF capacitors between the MOSFET, after five stages multiplying, the output voltage on the 150 ohm load is 1.1 kV with 100 ns pulse duration time and 100 Hz repetition rate.

The prototype of the pulse generator built on PCBs is shown in Figure 4.4. Each PCB has a two-stage Marx Bank. The BNC cable can easily add up the stages between the boards by connecting the output of the board with the lower stage (the rightmost BNC on the board) to the drive port of the board (the middle NBC on the board) with higher stage numbers. Figure 4.4 only shows a five-stage Marx Bank, however, more stages can be added up in this way by connecting more boards. The maximum voltage limitation of the cable must be considered. The output voltage to be coupled to the next board should not exceed the breakdown voltage of the cables.

The output of the Marx Bank prototype is tested as shown in Figure 4.5. Variation of the output voltage can be controlled by adjusting the stage number and the charging voltage. The trigger signal pulse width determines the on-time of the MOSFET and can eventually control the final output pulse width. The pulse width is also affected by the load impedance, and the final stage's capacitance, which forms an RC circuit. Therefore, the

fall-time of the pulse is determined by the switch-on time of the MOSFET, and the rise-time of the pulse is determined by the RC time constant.

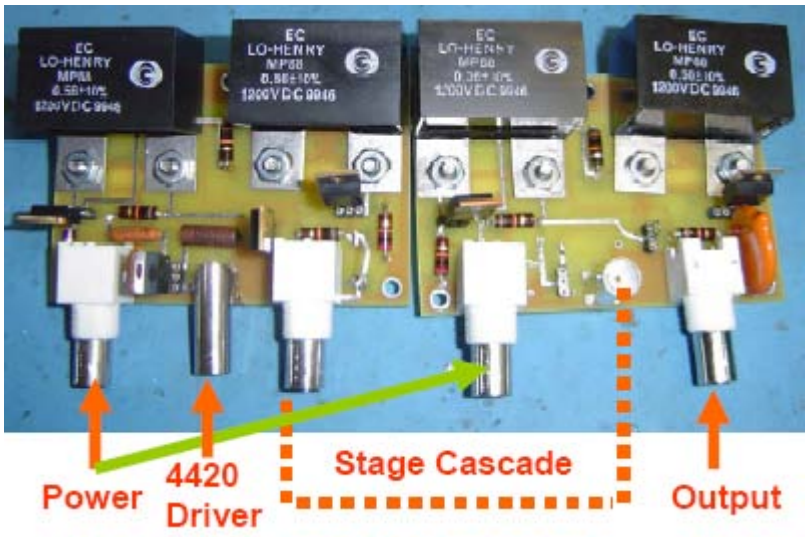

Figure 4.4 Prototype of the Marx Generator. The charging voltage is applied to the generator through the leftmost BNC of each PCB. 4420 driving circuit (see Appendix A) is used to provide the amplified trigger signal to the Marx. The output of the first board is coupled to the driver input of the second board.

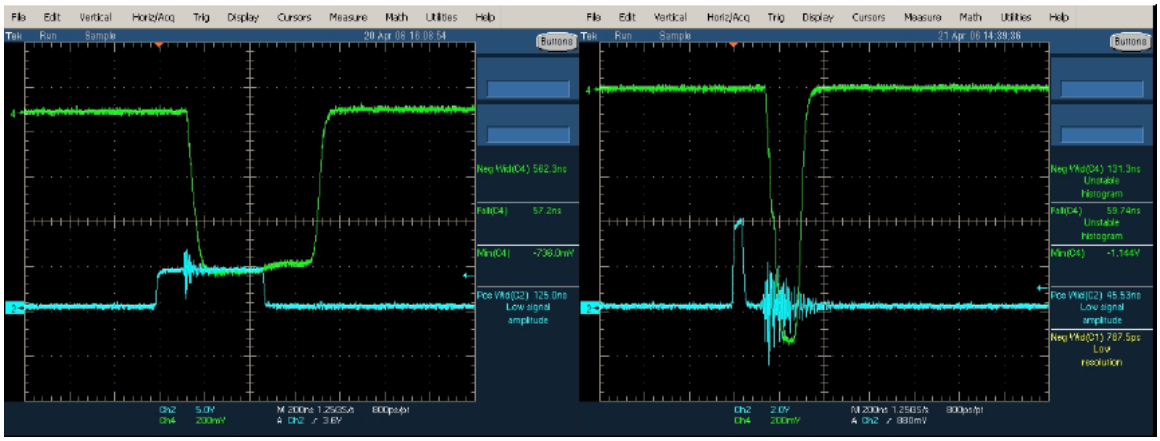

Figure 4.5 Waveform measurement of the Marx Generator. The green line is the output voltage on the load, the light blue is the trigger signal. The left graph is the three-stage Marx with 200 V charging voltage and 90 ohm load. Trigger pulse width of 500 ns results in 562 ns output voltage at 736 V. The right graph is the five-stage Marx with 200V input charging voltage with 90 ohm load. 45ns trigger single pulse width lead to a 131 ns output pulse width and 1144 V voltage.

4.2 Magnetic compression and diode opening switch pulse generator for car engine combustion

4.2.1 Principle of magnetic compression

The magnetic compression technique uses the non-linear properties of magnetic materials to achieve a very large change in inductance, resulting in large variation in current impedance. Typically, a large impedance comes with a large inductance when the magnetic core is unsaturated, while a small impedance comes with the small inductance when the magnetic core saturates. A little bit of background about magnesium is necessary to understand the mechanics of this technology. The Magnetic flux density B varies with magnetic field strength. If the relationship between the two is plotted for increasing levels of field strength, as is shown in Figure 4.6, it follows a curve up to a point where further increases in magnetic field strength will result in no further change in flux density (point B). This condition is called magnetic saturation. The relationship of B = μH is maintained before saturation happens. After reaching the saturation point, if the magnetic field is then reduced linearly, the plotted relationship will follow a different curve back towards zero field strength; this is called magnetic hysteresis.

Since the inductor has the ability to resist the change of the current, the inductive magnetic coil can block the current for a certain time, which works like a “switch-off” as in the normal switches. When the inductor gets saturated, B does not change with H (see

region III in Figure 4.6) and inductor cannot block the current anymore, therefore the saturated inductor works like “switch-on”. Figure 4.7 illustrated the operation of the magnetic switch. When C1 is charged up and the L is unsaturated, no current flows into C2. Since the L is designed to saturate at the voltage peak on C1, it then transfers all the stored energy in C1 to C2. Full energy transferring requires C1 = C2 = C. If we replicate the magnetic compression structure in Figure 4.7 and extend it to multiple stages as in Figure 4.8, when C2 is charged up, it can also be designed to release the energy to the next stage at the voltage peak, and so on and so forth.

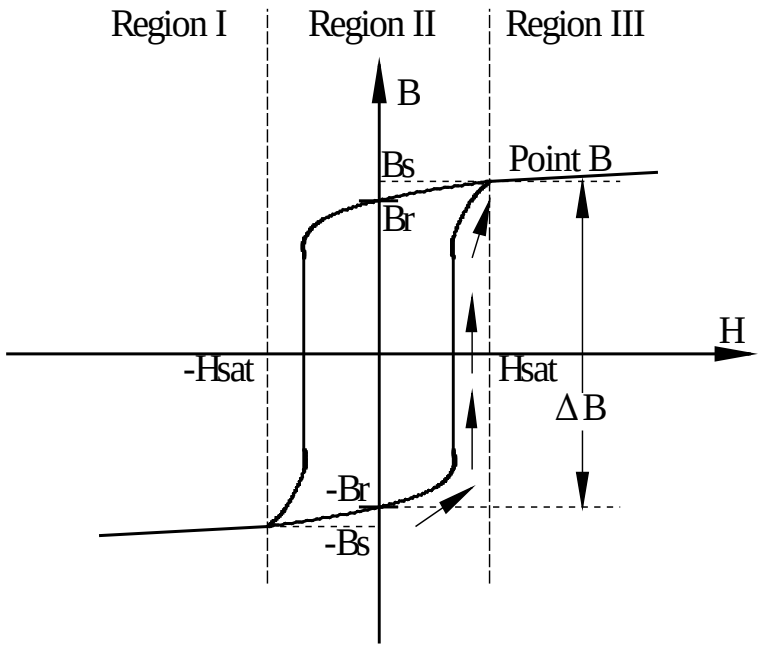

Figure 4.6 Magnetic hysteresis loop. H is the magnetic field strength and B is the magnetic flux density.

The saturated inductance can be calculated as:

$$L_{sat} = \mu_{sat}\mu_0 N^2 A / l \tag{4.4}$$

Here, N is the turn number of the inductor, A is the cross-section of the magnetic flux loop, and l is the length of the magnetic flux loop.

When the inductor gets saturated in the forward direction, it is still unsaturated in the reverse direction; therefore, the inductor acts as a diode to prevent reverse current flow back into the previous stage [Smith 1990]. In this case, C1, C2 and L are in series to form an LC resonant circuit, in which

$$t_{discharge C1} = t_{dis} = t_{charge C2} = \pi\sqrt{L\frac{C}{2}} \tag{4.5}$$

The saturation time for C1 can be determined by

$$t_{sat} = N\Delta BA / < V_C > \approx 2N\Delta BA / V_{peak} \tag{4.6}$$

Here, $<V_c>$ is the average voltage on the capacitor during the charging time, which is about half of the peak voltage at the capacitor.

In the magnetic compression topologies, there are several stages of inductors in cascade, as shown in Figure 4.8, and the inductors are sized with successively smaller values of

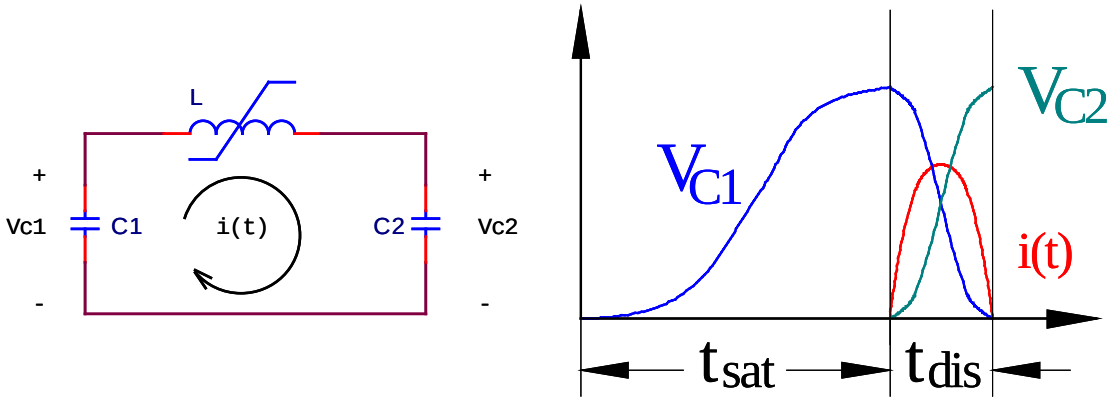

Figure 4.7 One stage of typical magnetic compression circuit

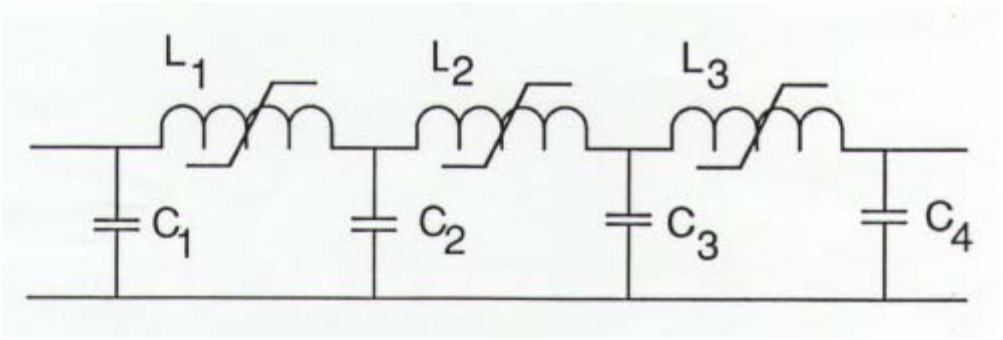

Figure 4.8 Schematic of three-stage magnetic compression circuit

saturated inductance such that for a given capacitor t_{sat} is 3~5 times longer than $t_{discharge.}$ So, only 3 stages are able to compress microsecond pulse width down to the nanosecond range.

4.2.2 Principle of diode opening switch

The diode opening switch (DOS) is also sometimes called a solid state opening switch (SOS). With the special P-N junction doping profile in the power diode, the turning-off process in the reversed biased diode can work as an opening switch. A practical high power P-N junction diode is shown in Figure 4.9. The N- layer, often called the drift region, is the prime feature not found in low-power diodes. Its function is to absorb the depletion layer of the reverse biased diode. When the diode is forward-biased, the P-N junction injects holes into the n-type drift region, and the hole space charge is large enough to attract electrons from the n+ region into the drift region. In this way the excess carriers are stored in the drift region. During the turn-off state, the excess carriers must be removed before the junction bias can be reversed, and the current goes negative and then the carriers are swept out to reduce the excess-carrier density [Moha 2003]. The diode can be modeled as the charge and discharge of the capacitor. If the forward charge pumping time is too long, the depletion region gets saturated and the “discharging” time is long, resulting in a slow switching speed of the diode. If the forward pumping time is

too short, less charge is stored in the depletion region and less reversed current is released.

A basic circuit schematic of the SOS switching scheme is given in Figure 4.10 [Kuthi 2005]. Switches S1 and S2 can be saturable inductors. Initially, S1 is open and S2 closed, and C1 is charged up. Afterward, S1 closes and S2 opens, and C1 then discharges into C2; forward current flows through the diode and charge is stored in the depletion layer of the diode. At the end of the diode forward biased cycle, S2 closes. The current through the SOS, I2-diode, reverses rapidly, eventually opening the SOS. The current finds nowhere to go but through the load as I2-commuted, as shown in Figure 4.10. The energy stored in C2 is then diverted to the load. The peak output voltage is determined as I2-commuted (diode reversed peak current) multiplies the load resistance.

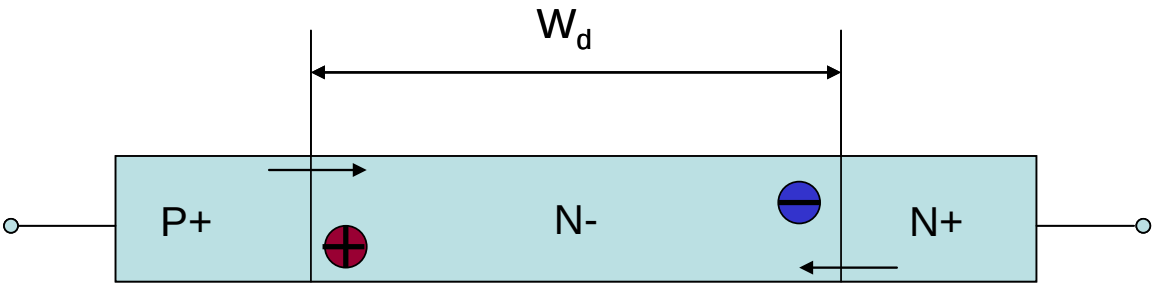

Figure 4.9 P-N junction of typical high power diode for DOS applications.

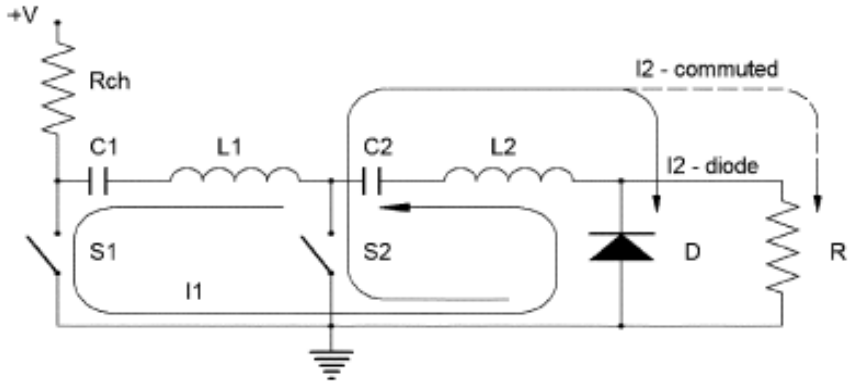

Figure 4.10 Operation principle of diode opening switch. [Kuthi 2005]

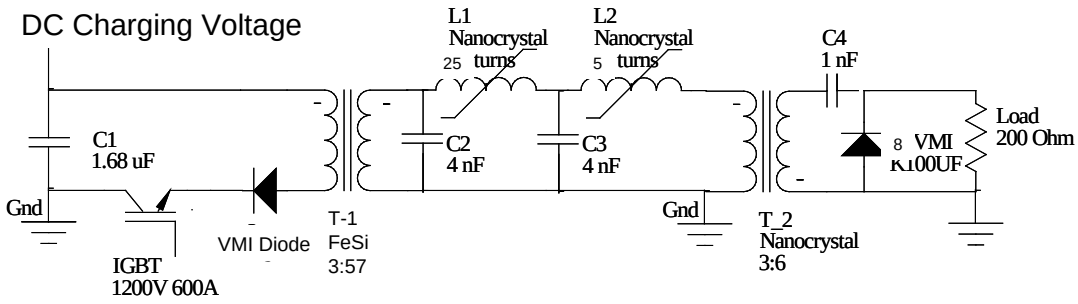

Figure 4.11 Circuit diagram of the magnetic compression pulse generator with diode opening sharpening at the output

4.2.3 Circuit design

The pulse generator built for the car engine combustion application is accomplished by applying three stages of saturable magnetic pulse width compression. Figure 4.11 shows the circuit design for the pulse generator that is able to output an 80 kV, 20 ns pulse into a 200 ohm load. In this circuit, a one kV dc voltage charges up the 1.68 μF capacitor bank C1. When the FUJI IGBT (rating at 1200 V, 600 A) switches, the energy is transferred through the 3:57 transformer T-1 to C2 with 4 nF capacitance. The turn ratio of the transformer is determined by optimizing the energy delivery when C1:C2 = $N2^2$:$N1^2$, in which N1 and N2 are the primary and secondary turn numbers of the transformer, respectively. At the same time, N1 should be large enough to prevent the saturation of the transformer before the expected voltage can be achieved on the secondary winding. A larger N1 number also works, but results in a larger number on the secondary, which may cause practical difficulties during winding. L_1, L_2 and T-2 are wound on a 2” OD, 1” ID, 1” high, finemat nanocrystal core from MK-Magnetics. The number of turns in L_1, L_2 are 25 and 5 turns respectively, which is carefully tuned so that they will saturate one after the other once C_2 and C_3 have charged to the peak value. T-2 is a saturable transformer with 3:6 turn ratio, which works as the third stage of magnetic compression. At the same time, it doubles the peak voltage on C4. A 1 nF capacitance is chosen for C4 to ensure that the maximum energy is delivered from C3 to C4. The DOS is in parallel with the

load, formed by 8 VMI K100UF diodes in series. The rated hold-off voltage of each diode is 10 kV and the current rating is 1.5 A dc.

As an example, the steps of the calculation are presented below to show the determinations of the parameters in the circuit. The calculation typically begins at the output port and flows towards to the input port. It is a good staring point for component choosing. However, the calculation numbers are subjected to change based on the real circuit tuning.

We need 80 kV peak voltage through 200 Ω load, therefore, the peak current through the load is:

$$I_o = \frac{V_o}{R_{load}} = 400A \tag{4.7}$$

And the total energy delivered in 20 ns pulse is:

$$E_o = \frac{1}{2} V_o I_o t = \frac{1}{2} \times 80 \times 10^3 \times 400 \times 20 \times 10^{-9} = 0.32J \tag{4.8}$$

The diode turn-off time determine the rising time of the output pulse. And the falling time of the output pulse is determined by time constant in the output circuit which is a serial RLC circuit. The L comes from the secondary inductance of the saturated transformer T-2. If we assume the shape of the output pulse is symmetric, and then the falling time is half the pulse width, and the saturated inductance of T-2 can be expressed as:

$$\frac{L_{satT2}}{R_{load}} = t$$
$$L_{satT2} = R_{load} t = 200 \times 20 \times 10^{-9} = 4\mu H \tag{4.9}$$

A quarter period of the $R_{load}L_{satT2}C_4$ oscillation from the output loop should be shorter than the diode recovery time of the diode, which is typical around 50 ns. Therefore:

$$\frac{\pi}{2}\sqrt{L_{satT2}C_4} = t_{diode}$$
$$C_4 = \left(2\frac{t_{diode}}{\pi}\right)^2 L_{satT2}{}^{-1} \approx 1nF \tag{4.10}$$

The similar procedure is processed for achieving the value for capacitor and saturated inductor for the previous stages.

Since we are using the finemat nanocrystal core on T-2 with a 2” OD, 1” ID, 1” high, we can calculate the turn number that is need to wound on the secondary.

$$L_{satT2} = \frac{\mu_{sat}\mu_0 N^2 A}{l}$$
$$A = \frac{(OD - ID)}{2} \cdot h = 312.5mm^2 \tag{4.11}$$
$$l = \frac{OD + ID}{2} \cdot \pi = 125.7mm$$

In which OD is the outside diameter of the core, ID is the inside diameter of the core, h is the thickness of the core. Then we need 25 turns on the secondary T-2. This number is larger than the number at the final circuit. The variation comes from the parasitic

inductance from the wiring in the loop inductance and the over estimated plasma load impedance.

Steps can be repeated for the previous stages of the circuit to guide the determination of the component parameters.

Figure 4.12 shows the prototype of the magnetic compression pulse generator with the diode opening switch at the final stage. This pulse generator is connected to a 1000 V DC power supply via the BNC at the “DC charge” port. A trigger signal is also needed for controlling the IGBT. The diode chain is designed with banana plugs that can be

Figure 4.12 Prototype of the pulse generator, a “plug in” diode testing interface is designed as shown in the right hand graph.

connected to the banana jacks on the back panel of the pulse generator. This way, the installation of the diode chain becomes very easy.

The output voltage of the pulse generator is shown in Figure 4.13. The pulse waveform is measured with 1 kV charging voltage and a 200 ohm load. The output amplitude is 66.8 kV measured through a 1:1000 voltage divider. The pulse width is 14.5 ns. Because of the lack of saturable inductors resetting circuit [Barrett 1995], the cores are not biased at the negative saturation flux on its B-H curve at the beginning for each pulse generation. Therefore, the output of the pulse generator is not very stable. The amplitude of the pulse voltage changes shot to shot with a deviation of 5.47 kV.

This pulse generator was successfully used to ignite the 1” gap spark plug by producing the transient plasma streamers. The picture on the left in Figure 4.14 shows the undesirable arc generated in the spark plug. The picture on the right in Figure 4.14 is the plasma streamer image produced by the pulse generator. Streamers lead to better combustion, higher power efficiency and less emission of polluting chemicals.

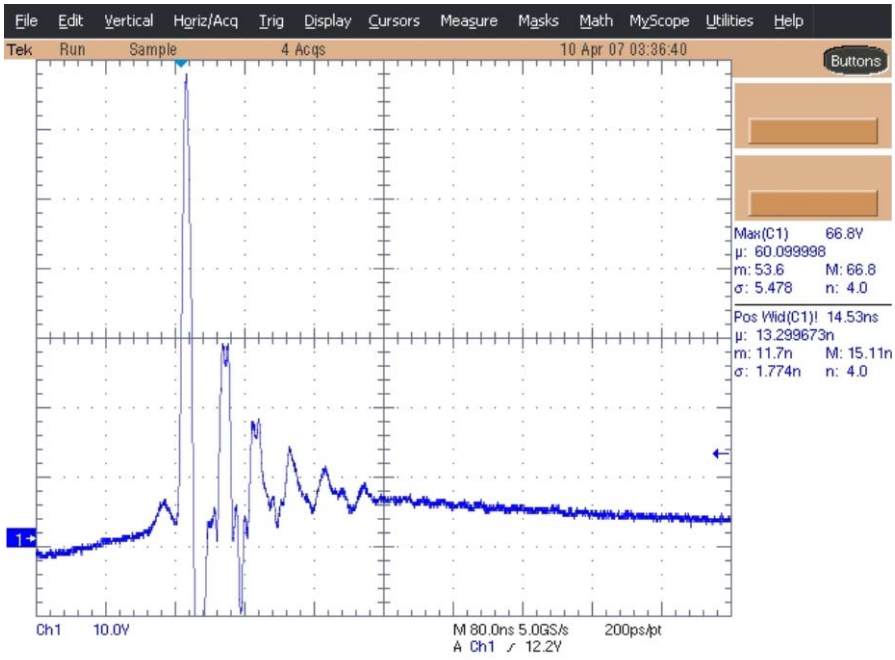

Figure 4.13 Voltage waveform of the pulse generator.

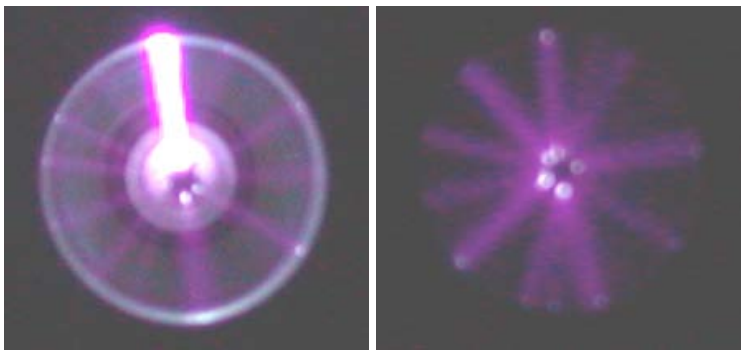

Figure 4.14 Streamer is generated in 1 inch gap spark plug by the DOS generator. Left side shows the arc produced after the transient plasma streamers.

4.3 Chapter 4 summary

Solid state pulsed power systems have drawn special attention due to their superior properties in compactness, light weight, low cost, and high efficiency. Various semiconductor switching units have become commercially available and have been used in various pulsed power applications. In this chapter, the power MOSFET switched Marx generator and the magnetic pulse width compression generator with the diode opening switch are introduced. The Marx generator is designed for the skin cancer cell electroporation experiment wherein the cancer cells are loaded into the microchamber with equivalent impedance of 150-200 ohm. The five-stage self-triggered Marx Bank is able to multiply 200 V input voltage five times to the output voltage. A 1 kV, 130 ns pulse

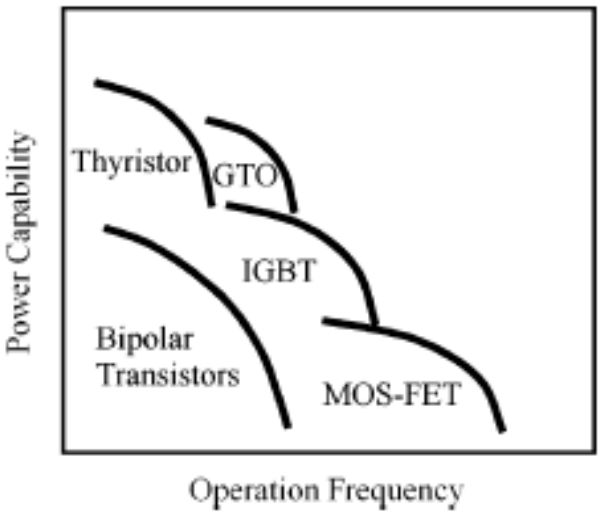

Figure 4.15 Relative power and frequency capabilities of different semiconductor switches [Jiang 2004].

is measured on a 200 ohm load resistor, which meets the design requirement for the microchamber experiments. The magnetic pulse compression generator uses three compression stages and one reversed diode sharpening stage to achieve a 60 kV peak voltage pulse with 20 ns pulse width. This pulse generator successfully produces the plasma streamers in the 1 inch gap ignition plug for the car engine combustion experiments.

As a summary, it is obvious that different types of solid state switches are used in different ways, operated with different parameter, and employed for different applications. This chapter only covers a small portion of their wide range of applications. Figure 4.15 from reference [Jiang 2004] shows the relative operation frequency and power capability of the different power semiconductors. Among the power semiconductors, the thyristor has a relatively long history and high power capability. However, once it is turned on, it remains latched in the on-state as long as the anode remains positively biased. It cannot be switched off until the anode current falls below the holding current. Its slow turn-off speed limits its operation frequency to be in the order of 100 Hz or lower. The gate turn-off thyristor (GTO) can be turned on as well as off via the application of a gate drive. The insulated-gate bipolar transistor (IGBT) has advantages in both high-power capability (high current) and high operation frequency. Nowadays, it is the most popular semiconductor switch for kilohertz-level pulsed power generators. The

metal–oxide–semiconductor field-effect transistor (MOSFET) has the fastest speed and is widely used for very high frequency operations (up to the megahertz level), although its power capability is comparatively lower than the other semiconductor switches.

Chapter 5: Conclusions

The fundamental purpose of all pulsed power systems is to convert a low-power, long-time input into a high-power, short-time output. This dissertation focuses on several topics in the high voltage pulsed power field, including the development of plasma switches, circuit design, and their applications in plasma device systems. Although each topic looks independent of one another, they are connected based on the pulsed power technology, especially the nanoseconds-range pulsed power.

Chapter 1 mainly introduces the frame of the pulse power system which includes five main parts: power source, energy storage, pulse compression, impedance match network and load. Each part plays a role in the pulsed power system. In order to obtain nano-second range high power pulse, the power switches and circuit topologies are especially critical. The regular parameters of the switch characterization are introduced in this chapter. The plasma wakefeild accelerator was briefly demonstrated as one of the applications of pulsed power technology.

Chapter 2 discusses the development of the mini back-lighted thyratron (BLT), a gas type high power switch, and its applications in the portable power generator for car engine

ignition. The mini BLT is able to hold-off 40 kV voltage by limiting the scale of pressure • gap (Torr • cm) below Paschen's gas (hydrogen or helium) breakdown voltage. This switch is optically controlled by the UV light, which generate the photo-electrons to initialize the plasma channel formation between the electrodes and therefore, triggers the "turn-on" of the switch. It is clear that higher optical energy can produce more "seed" electrons, and results in lower switching delay and jitter. Models of the hollow cathode are introduced, explaining the high current conducting capability of the mini-BLTs. As high as 4.5 kA peak current with 10 ns switch-on time and 10^{11} A/s current rise rate was observed during the operation of the switch. With its size—comparable to a human finger and much smaller than the conventional pseudospark—the mini-BLT has a huge potential to be applied in portable pulse power machines.

The recognition that the hollow-cathode structure of the BLT is the key for its high current conducting capability is what inspired the idea to produce high density plasma. This was the original idea for creating the source for the plasma accelerator that requires high plasma densities. Although the final experiment results revealed that the hollow cathode didn't obviously help the gas ionization with gas pressure around one atmosphere, a way to increase the plasma density above 10^{19} cm^{-3} by making hydrogen discharge in the capillary was explored. Chapter 3 discusses the development of a high density plasma capillary source for plasma wakefield applications. The borosilicate capillary tube is

filled with hydrogen. A pseudospark pulse generator applies a 60 kV, 800 A, 100 ns pulse to ionize the hydrogen. The geometry (radius, length) of the capillary and gas pressure were varied and spectroscopic and electrical analysis were performed to characterize the plasma. This low cost, repeatable and controllable plasma source is believed to be able to lead a resonant excitation of the plasma wakefield and generate a several GeV/m acceleration gradient in the plasma wakefield accelerator scheme.

Besides the applications of the gas type switches, there is another main type of pulsed power that is composed of pure solid state components. Although the solid state switches are typically slower than the gas switches and lack the strong capabilities of handling high power, they benefit from their low-cost, small-size and lower maintenance requirements. Carefully designing the circuit and using an array of the semiconductor switches can make up for their short comings. They are becoming the most popular pulsed power systems nowadays. Chapter 4 introduces two pure solid state pulse generators: the Marx Bank generator, the Magnetic pulse width compression, and the diode opening switch pulse generator. They are designed and built for skin cancer cell treatment applications, as well as for transient plasma streamer car engine ignition applications.

After exploring the pulsed power devices mentioned above, there is still a lot that can be done for their improvement, and for new explorations. The mini-BLT will be brazed and

sealed. A triggering light source other than the laser is sought after to further reduce the total system size and cost. The capillary plasma source will be applied in real accelerator experiments. The high intensity light emission from the gas discharge in the capillary may be developed as a novel lighting source. And a sub-nanosecond solid state pulse generator is under investigation, which is expected to produce an electrical field that is fast enough to penetrate the inner part of the cancer cells.

Bibliography

[Anders 1994] Anders, A. and Anders, S., “Electron Emission from Pseudospark Cathodes,” J. Appl. Phys., Vol. 76, No. 3, pp. 1494-1502, Aug., 1994.

[Anders 1993] Anders, A., Anders, S. and Gundersen, M. A., “Model for Explosive Electron Emission in a Pseudospark Superdense Glow,” Phys. Rev. Lett., vol. 71, no. 3, pp. 364-367, Jul. 1993.

[Anders 1995] Anders, A., Anders, S., Gundersen, M. A. and Martsinovskii, A. M., “Self-Sustained Self-Sputtering: A Possible Mechanism for the Superdense Glow Phase of a Pseudospark,” IEEE Trans. Plasma Sci., vol.23, no. 3, pp. 275-282, Jun. 1995.

[Ashkenazy 1991] Ashkenazy, J., Kipper, R. and Caner, M., “ Spectroscopic measurements of electron density of capillary plasma based on Stark broadening of hydrogen lines”, Phys. Rev. A, vol. 43, pp. 5568-5574, 1991.

[Baker 1993] Baker, R. J., Johnson, B. P., “Applying the Marx Bank circuit configuration to power MOSFET”, Electro. Lett., vol 29, pp. 56-57, Jan 1993.

[Barrett 1995] Barrett, D. M., “Core reset considerations in magnetic pulse compression networks,” IEEE Pulsed Power Conference, pp.1160-1165, 1995.

[Bauer 1990] Bauer, H. R., Kirkman, G. and Gundersen, M. A., “A Tow-Component Model for the Electron Distribution Function in a High-Current Pseudospark or Back-Lighted Thyratron,” IEEE. Trans. Plasma Sci., Vol. 18, No.2 pp 237-245, Apr. 1990.

[Bekefi 1976] Bekefi, G., Principles of Laser Plasmas. New York: John Wiley & Sons, 1976.

[Bickel 1991] Bickel, P., Christiansen, J., Frank, K., Gortler, A., Hartmann, W., Kowalewicz, R., Linsenmeyer, A., Kozlik, C., Stark, R., and Wiesneth, P., "High-Repetition Rate Sealed-Off Pseudospark Switches for Pulsed Modulators," IEEE Trans. Plasma Sci., vol. 38, no. 4, pp. 712-716, Apr. 1991.

[Bingham 2007] Bingham, R., "On the crest of a wake", Nature, vol. 445, pp.721-722, 2007.

[Blumenfeld 2007] Blumenfeld, I., Clayton, C. E., Decker, F., Hogan, M. J., Huang, C., Ischebeck, R., Iverson, R., Joshi, C., Katsouleas, T., Kirby, N., Lu, W., Marsh, K. A., Mori, W. B., Muggli, P., Oz, E., Siemann, R. H., Walz, D., and Zhou, M., "Energy doubling of 42 GeV electrons in a meter-scale plasma wakefield accelerator", Nature, vol. 45, pp.741-744, 2007.

[Bobrova 2001] Bobrova, N. A., Esaulov, A. A., Sakai, J. I., Sasorov, P. V., Spence, D. J., Butler, A., Hooker, S. M., and Bulanov, S. V., "Simulations of a hydrogen-filled capillary discharge waveguide", Phys. Rev. E., vol. 65 p. 016407, 2001.

[Bochkov 2000] Bochkov, V. D., Korolev, Y. D., Frank, K., Frants, O. B. and Shemyakin, I. A., " Pseudospark switches for the power supply circuits of pulsed lasers", Russian Phys. Jour. vol. 43, no. 5, pp. 432-439, 2000.

[Boeuf 1991] Boeuf, J. and Pitchford, L. C. "Pseudospark discharges via computer simulation," IEEE Trans. Plasma Sci., vol. 19, no. 2, pp. 286-296, Apr. 1991.

[Braun 1988] Braun, C., Hartmann, W., Dominic, V., Kirkman, G., Gundersen, M. and Mcduff, G., "Fiber-optic-triggered high-power low-pressure glow discharge switches", IEEE Trans. Electron Device, vol. 35, 559, 1988.

[Braun 2003] Braun, H. H., Dobert, S., Wilson, I. and Wuensch, W. “Frequency and Temperature Dependence of Electrical Breakdown at 21, 30, and 39 GHz,” Phys. Rev. Lett., Vol. 90, p. 224801, 2003.

[Broks 2005] Broks, B. H. P., Garloff, K., and van der Mullen, J. J. A. M., “Nonlocal-thermal-equilibrium model of a pulsed capillary discharge waveguide”, Phys. Rev. E., vol. 71, p. 016401, 2005.

[Butler 2002] Butler, A., Spence, D. J. and Hooker, S. M., “Guiding of high-intensity laser pulses with a hydrogen-filled capillary discharge waveguide”, Phys. Rev. Lett., vol. 89, p. 185003, 2002.

[Cetiner 2008] Cetiner, S. O., Stoltz, P., Messmer, P. and Cambier J., “Dependence of electron peak current on hollow cathode dimensions and seed electron energy in a pseudospark discharge”, J. Appl. Phys. 103, 023304, 2008.

[Cherrington 1982] Cherrington, B. E., “The Use of Electrostatic Probes for Plasma Diagnostics – A Review,” Plasma Chem., Plasma Proc.,Vol. 2. no.2, pp.113-140, 1982.

[Christiansen 1979] Christiansen, J. and Schultheiss, C., “Production of high current particle beams by a low pressure spark discharge,” Z. Phys., vol. A-290, pp. 35, 1979.

[Clayton 2002] Clayton, C. E, Glue, B. E., Dodd, E. S., Joshi, C., Marsh, K. A., Mori, W. B., Wang, S., Catravas, P., Chattopadhyay, S., Esarey, E., Leemans, W. P., Assmann, R., Decker, F. J., Hogan, M. J., Iverson, R., Raimondi, P., Siemann, R. H., Walz, D., Katsouleas, T., Lee, S. and Muggli, P., “Transverse envelope dynamics of a 28.5-GeV electron beam in a long plasma”, Phys. Rev. Lett., vol. 88, p. 154801, 2002.

[Crouch 1972] Crouch, J. H. and Risk, W. S., “A Compact High Speed Low Impedance Blumlein Line for High Voltage Pulse Shaping,” Rev. Sci. Instrum., Vol. 43, P. 632, 1972.

[D’Agostino 2008] D’Agostino, R., Favia, P., Kawai, Y., Ikegami, H., Sato, N., and Arefi-Khonsari, F., Advanced Plasma Technology, Wiley-Vch, 2008.

[Davis 1983] Davis, G. P. and Gottscho, R. A., “Measurement of spatially resolved gas-phase plasma temperatures by optical emission and laser-induced fluorescence spectroscopy,” J. Appl. Phys., Vol.54, no.6, pp. 3080-3086, June 1983.

[Deng 2003] Deng, S. , Barnes, C. D. , Clayton, C. E. , O’Connell, C. , Decker, F. J. , Erdem, O. , Fonseca, R. A. , Huang, C. , Hogan, M. J. , Iverson, R. , Johnson, D. K. , Joshi, C. , T. Katsouleas, Krejcik, P. , Lu, W. , Marsh, K. A. , Mori, W. B. , Muggli, P. , and Tsung, F. "Plasma wakefield acceleration in self-ionized gas or plasmas", Physical Review E 68, vol. no.4, p. 047401, 2003.

[Eichhorn 1993] Eichhorn, H., Schoenbach, K. H. and Tessnow, T., “Paschen’s law for a hollow cathode discharge” Appl. Phys. Lett., vol. 63, pp. 2481-2483, Vol. 63, No. 18, Nov. 1993.

[Fiocco 1963] Fiocco, G. and Thompson, E., “Thomson sacattering of optical radiation from an electron Beam,” Phys, Rev. Lett., Vol. 10, no.3, pp 89-91, Feb. 1963.

[Frank 1988] Frank, K., Boggasch, E., Christiansen, J., Goertler, A., Hartmann, W., Kozlik, C., Kirkman, G., Braun, C., Dominic, V., Gundersen, M. A., Riege, H. and Mechtersheimer, G., “High-power pseudospark and BLT switches,” IEEE Trans. Plasma Sci., vol. 16, no. 2, pp. 317-323, Apr. 1988.

[Frank 2007] Frank, K., Petzenhauser, I., and Blell, U., “Multi-gap pseudospark switches for high voltage applications,” IEEE Trans. Dielectr. Electr. Ins., vol. 14, no. 4, pp. 968-975, Aug. 2007.

[Galindo 2008] Galindo, F. G., Vernier, P. T., Dejmek, P., Vicente, A., and Gundersen, M. A., “Pulsed electric field reduces the permeability of potato cell wall,” Bioelectromagnetics, Vol. 29, No. 4, pp. 296-301, May, 2008

[Garon 2007] Garon, E. B., Sawcer, D., Vernier, P. T., Tang, T., Sun, Y., Marcu, L., Gundersen, M. A., and Koeffler, H. P., “In vitro and in vivo evaluation and a case report of intense nanosecond pulsed electric field as a local therapy for human malignancies,” Int. J. Cancer 121, pp. 675-682, 2007.

[Geddes 2004] Geddes, C. G. R., Toth, Cs., van Tilborg, J., Esarey, E., Schroeder, C. B., Bruhwiler, D., Nieter, C., Cary, J., Leemans, W. P., “High-quality electron beams from a laser wakefield accelerator using plasma-channel guiding”, Nature, vol. 431, pp. 538-541, 2004

[Geddes 2005] Geddes, C. G. R., Toth, Cs., Van Tilborg, J., Esarey, E., and Schroeder, C. B., Bruhwiler, D., Nieter, C., and Cary, J., and Leemans, W. P., “Production of high-quality electron bunches by dephasing and beam loading in channeled and unchanneled laser plasma accelerators”, Phys. Plasma, vol. 12, p. 056709, 2005.

[Gonsalves 2007] Gonsalves, A. J. , Rowlands-Rees, T. P. , Broks, B. H. P. , van der Mullen, J. J. A. M. , and Hooker, S. M. , “Transverse Interferometry of a Hydrogen-Filled Capillary Discharge Waveguide”, Phys. Rev. Lett. vol. 98, no.2, 025002, 2007.

[Granovsky 1971] Granovsky, V. L., Electric Current in Gas (Steady Current). Moscow: Nauka, 1971.

[Griem 1974] Griem, H. R., “Spectral line broadening by plasma”, Academic, New York, 1974

[Gutler 2002] Gutler, A., Spence, D. J. and Hooker, S. M., “Guiding of high-intensity laser pulsed with a hydrogen-filled capillary discharge waveguide”, Phys. Rev. Lett., vol. 28, p. 185003, 2002.

[Hartmann 1988] Hartmann, W. and Gundersen, M. A., “Origin of anomalous emission in superdense glow discharge,” Phys. Rev. Lett., vol. 60, no. 23, pp. 2371-2374, Jun. 1988.

[LHC] http://www.interactions.org/LHC.

[Hutchinson 2002] Hutchinson, I. H., Principles of Plasma Diagnostics, Cambridge University Press, 2002.

[Jacobs 2007] Jacobs, B., Gekelman, W., Pribyl, P., Barnes, M., Kilgore, M., “Laser-induced Fluorescence measurements in an inductively coupled plasma reactor,” Appl. Phys. Lett. Vol. 91, P. 161505, 2007.

[Jiang 2005] Jiang, C., Kuthi, A. and Gundersen, M. A., “Toward ultracompact pseudospark switches,” Appl. Phys. Lett., vol. 86 pp. 024105, 2005.

[Jiang 2004] Jiang, W., Yatsui, K., Takayama, K., Akemoto, M., Nakamura, E., Shimizu, N., Tokuchi, A., Tukin, S., Tarasenko, V., Ranchenko, A., “Compact solid-state switched pulsed power and its applciaitons,” Proceeding of the IEEE, vol. 92, pp. 1180-1196, July, 2004.

[Kallos 2008a] Kallos, E., Plasma Wakefield Accelerators Using Multiple Electron Bunches, Doctoral thesis, University of Southern California, 2008.

[Kallos 2008b] Kallos, E., Katsouleas, T., Kimura, W. D., Kusche, K., Muggli, P., Pavlishin, I., Pogorelsky, I., Stolyarov, D. and Yakimenko, V., “High-Gradient Plasma-Wakefield Acceleration with Tow Subpicosecond Electron Bunches”, Phys. Rev. Lett., Vol. 100, p. 074802, 2008.

[Kallos 2005] Kallos, E., Katsouleas, T., Muggli, P., Ben-Zvi, I., Pogorelsky, I., Yakimenko, V., Pavlishin, I., Kusche, K., Zhou, F., and Kimura, W. D., "A Multibunch Plasma Wakefield Accelerator", Proceedings of 2005 Particle Accelerator Conference, Knoxville, TN, pp.3384-3386, 2005.

[Kim 2006] Kim, G. J., Iza, F. and Lee, J. K., “Electron and Ion Kinetics in a Micro Hollow Cathode Discharge,” J. Phys. D:Appl. Phys. Vol.39, pp. 4386-4392, 2006.

[Kim 2008] Kim, G. J. and Lee, J. K., “Pendulum Electrons in Micro Hollow Cathode Discharges,” IEEE. Trans. Plasma Sci., Vol. 36, No. 4, pp. 1238-1239, Aug. 2008.

[Kirkman 1986] Kirkman, G. F. and Gundersen, M. A., “Low Pressure, Light Initiated, Glow Discharge Switch for High Power Applications,” Appl. Phys. Lett. vol. 49, pp. 494-495, Sep. 1986.

[Kosner 1997] Kosner, M. A., Bender, H. A., Sifvast, W. T. and Rocca, J. J., “Intense plasma discharge source at 13.5nm for extreme-ultraviolet lighography”, Opt. Lett. Vol. 22, pp. 34-36, 1997.

[Kuthi 2005] Kuthi, A., Gabrielsson, P., Behrend, M. R., Vernier, P. T. and Gundersen, M. A., “Nanosecond Pulse Generator Using Fast Recovery Diodes for Cell Electromanipulation,” IEEE. Trans, Plasma Sci., vol. 33, No. 4, august 2005.

[Langmuir 1924] Langmuir, I., Mott-Smith, H, “Langmuir probe technique,” Gen. Electr. Rev. vol. 27, p. 449, 1924.

[Lee 2007] Lee, B. J., Rahaman, H., Petzenhauser, I., Frank, K. and Giapis, K. P., “Xenon excimer emission from pulsed high-pressure capillary microdischarges,” Appl. Phys. Lett., vol. 90, p. 24502, 2007

[Lawrence 1932] Lawrence, E. O. and Livingston, M. S., “The Production of High Speed Light Ions Without the Use of High Voltages,” Phys. Rev. Lett., Vol. 40, no.1, PP. 19-35, 1932.

[Levin 2005] Levin, M., Pukhov, A., Hubbard, F. F., Kaganovich, D., Gordon, D. F., Sprangle, P., Ting, A., Hafizi, B., Zigler, A., “Longitudinal profiles of plasma parameters in a laser-ignited capillary discharge and implications for laser wakefield accelerator applications”, Appl. Phys. Lett., vol. 87, p. 261501, 2005.

[Lin 1995] Lin, B. and Chow, Q., “Breakdown voltages of pseudospark in He, A, and N2,” IEEE Trans. Plasma Sci., vol. 23, no. 3, pp. 239-242, Jun. 1995.

[Liu 2005] Liu, J. B., Wang, F., Li, G., Kuthi, A., Gutmark, E. J., Ronney, P. D., and Gundersen, M. A., “Transient Plasma Ignition,” IEEE Trans. Plasma Sci., Vol. 33, No. 2, pp. 326-327, April 2005.

[Lochte-Holtgreven 1976] Lochte-Holtgreven, W., “Nuclear fusion in very dense plasmas obtained from electrically ‘exploded’ liquid threads”, Atomkernenergie, vol. 28, pp.150-154, 1976.

[Lu 2005] Lu, W., Huang, C., Zhou, M. M., Mori, W. B., and Katsouleas, T., “Limits of linear plasma wakefield theory for electron or positron beams”, Phys. Plasmas, vol. 12, p. 063101, 2005.

[Luther 2005] Luther, B. M., Wang, Y., Berrill, M., Alessi, D., Marconi, M. C., Latrotonda, M. A. and Rocca, J. J., “Highly ionized Ar plasma waveguides generated by a Fast Capillary Discharge”, IEEE Trans. Plasma Sci., vol. 33, pp. 582-583, 2005.

[Mallik 1999] Mallik, K., “The theory of operation of transistorized Marx bank circuits”, Rev. Sic. Instrum., Vol. 70, No. 4, pp. 2155-2160, April, 1999.

[Mangles 2004] Mangles, S. P. D., Murphy, C. D., Najmudin, Z., Thomas, A. G. R., Collier, J. L., Dangor, A. E., Divall, E. J., Foster, P. S., Gallacher, J. G., Hooker, C. J., Jaroszynski, D. A., Langley, A. J., Mori, W. B., Norreys, P. A., Tsung, F. S., Viskup, R., Walton, B. R., Krushelnick, K., “Monoenergetic beams of relativistic electrons from intense laser–plasma interactions”, Nature, vol. 431, pp. 535-538, 2004.

[Mankowski 2008] Mankowski, J., Kristiansen, M., “A Review of Short Pulse Generator Technology,” IEEE Trans. Plasma Sci., Vol. 28, No. 1, pp. 102-108, 2008.

[Martin 1990] Martin, T. H., Guenther, A. H. and Kristiansen, M., Gas Discharge Closing Switches, New York: Plenum Press, 1990.

[Martin 1996] Martin, T. H., Guenther, A. H., Kristiansen, M., Martin, J. C. on Pulsed Power, New York: Plenum Press, 1996.

[Mehr 1995] Mehr, T., Arenz, H., Bickel, P., Christiansen, J., Frank, K., Gortler, A., Heine, F., Hofmann, D., Kowalewicz, R., Schlaug, M. and Tkotz, R., "Trigger Devices for Pseudospark Switches", IEEE Trans. Plasma Sci. 23, 324, 1995.

[Moha 2003] Moha, N., Undeland, T. M., and Robbins, W., "Power Electronics", John Wiley & Sons, Inc., 2003.

[Morgan 1994] Morgan, C. A., Griem, H. R. and Elton, R.C., "Spectroscopic measurements of electron density and temperature in polyacetal-capillary-discarge plasmas", Phys. Rev. E, vol. 49, pp. 2282-2290, 1994.

[Muggli 2004] Muggli, P., Blue, B. E., Clayton, C. E., Deng, S., Decker, F. J., Hogan, M. J., Huang, C., Iverson, R., Joshi, C., Katsouleas, T. C., Lee, S., Lu, W., Marsh, K. A., Mori, W. B., O'Connell, C. L., Raimondi, P., Siemann, R. and Walz, D., "Meter-scale plasma-wakefield accelerator driven by a matched electron beam", Phys. Rev. Lett., Vol. 93, p. 014802, 2004.

[Muggli 2008] Muggli, P., Yakimenko, V., Babzien, M., Kallos, E. and Kusche, K. P., "Generation of trains of electron microbunches with adjustable subpicosecond spacing", Phys. Rev. Lett. , Vol. 101, p. 054801, 2008.

[Murphy 1956] Murphy, E. G. and Good, R. H., "Thermionic Emission, Field Emission and The Transition Region," Phys. Rev., Vol. 102, No. 6, pp. 1464-1473, June, 1956.

[Naweed 1999] Naweed, A., Kiefer, J., Rohner, M. and Neff, W., “Lifetime and Switching Characteristics of a High-Current Multichannel Pseudospark,” J. Appl. Phys., vol. 86, pp. 6673-6676, Dec. 1999.

[Pak 1992] Pak, H. and Kushner, M. J., “Breakdown characteristics in nonplanar geometries and hollow cathode pseudopsark switches,” J. Appl. Phys., vol. 71, pp. 94-100, Jan. 1992.

[Pancheshny 2000] Pancheshny, S. V., Sobakin, S. V., Starikovskaya, S. M., and Starikovskii, A. Y., “Discharge dynamics and the production of active articles in a cathode-directed streamer,” plasma phys. Rep. , vol. 26, no. 12, pp. 1054-1056, 2000.

[Panofsky 1999] Panofsky, W. K. H. and Breidenbach, M., “Accelerators and Detectors,” Rev. Mod. Phys., Vol. 71, pp. S121-S1312, 1999.

[Paschen 1889] Paschen, F., "Ueber die zum Funkenübergang in Luft, Wasserstoff und Kohlensäure bei verschiedenen Drucken erforderliche Potentialdifferenz," Annalen der Physik Vol. 273, No. 5, pp.69–75, 1889.

[Pitchford 1995] Pitchford, L. C., “Predicted Emittance and Brightness of the Pseudospark Electron-Beam,” IEEE Trans. Plasma Sci., vol. 23, no. 3, pp. 243-247, June 1995.

[Pritzkau 2002] Pritzkau, D. and Siemann, R., “Experimental study of rf pulsed heating on oxygen free electronic copper”, Phys. Rev. ST Accel. Beams, Vol. 5, p. 112002, 2002.

[Raizer 1997] Raizer, Y. P., Gas Discharge Physics. New York: Springer-Verlag, 1997.

[Raju 2006] Raju, G. G., Gaseous Electronics Theory and Practice. Taylor & Francis, 2006.

[Rocca 1993a] Rocca, J. J., Cortazar, O. D., Szapiro, B., Floyd, K. and Tomasel, F. G., " Fast- discharge excitation of hot capillary plasmas for soft-x-ray amplifiers", Phys. Rev. E , vol. 47, pp. 1299-1304, 1993.

[Rocca 1993b] Rocca, J. J., Cortazar, O. D., Tomasel, G. G. and Szapiro, B. T., " Efficient generation of highly ionized calcium and titanium plasma columns for collisionally excited soft-x-ray lasers in a fast capillary discharge", Phys. Rev. E, vol. 48, pp. R2378-R2381 ,1993.

[Rocca 1994] Rocca, J. J., Shlyaptsev, V., Tomasel, F. G., Cortazar, O. D., Hartshorn, D., and Chilla, J. L. A., "Demonstration of a Discharge Pumped Tabel-Top Soft-X-Ray Laser," Phys. Rev. Lett., Vol. 73, Oct., 1994.

[Rowlands-Rees 2008] Rowlands-Rees, T. P., Kamperidis, C., Kneip, S., Gonsalves, A. J., Mangles, S. P. D., Gallacher, J. G., Brunetti, E., Ibbotson, T., Murphy, C. D., Foster, P. S., Streeter, M. J. V., Budde, F., Norreys, P. A., Jaroszynski, D. A., Krushelnick, K., Najmudin, Z., and Hooker, S. M., "Laser-Driven Acceleration of Electrons in a Partially Ionized Plasma Channel", Physical Review Letters 100, no.10, p.105005, 2008

[Schoenbach 1997] Schoenbach, K. H., Peterkin, F. E., Alden, R. W., Beebe, S. J., "The Effect of Pulsed Electric Fields on Biological Cells: Experiments and Applications," IEEE Trans. Plasma Sci., vol. 25, No.2, pp. 284-292, April, 1997

[Sheffield 1975] Sheffield, J., Plasma Scattering of Electromagnetic Radiation (Academic Press, 1975)

[Smith 1990] Smith, C. H., "Applications of amorphous magnetic materials at very-high magnetization rate"' J. Appl. Phys. vol. 67, pp5556-5561, 1990.

[Smulders 1998] Smulders, E. H. W. M., van Heesch, B. E. J. M., and vann Paasen, S. S. V. B., "Pulsed Power Corona Discharges for Air Pollution Control," IEEE. Trans. Plasma Sci., Vol. 26, No. 5, pp. 1476-1484, Oct., 1998.

[Spence 1999] Spence, D. J., Burnett, P. and Hooker, S. M., “Measurement of the electron-density profile in a discharge-ablated capillary waveguide”, Optics Letters 24, no.14, 993, 1999

[Sun 2005] Sun, Y., Vernier, P. T., Behrend, M., Marcu, L., and Gundersen, M. A., "Electrode microchamber for non-invasive perturbation of mammalian cells with nanosecond pulsed electric fields," IEEE Trans. Nanobiosci., vol4, pp.277-283, 2005.

[Tang 2008] Tang, T., Design and Implementation of Full Solid State High Voltage Nanosecond Pulse Generators, Doctoral thesis, University of Southern California, 2008.

[Tang 2007] Tang, T., Wang, F., Kuthi, A., Gundersen, M. A., “Diode Opening Switch Based Nanosecond High Voltage Pulse Generators of Biological and Medical Applications,” IEEE Trans. Dielectr. Electr. Insul., Vol. 14, pp. 878-833, Aug., 2007.

[Taniyasu 2006] Taniyasu, Y., Kasu, M. and Makimoto, T., “An aluminum nitride light-emitting diode with a wavelength of 210 nanometers,” Nature, Vol. 441, pp325-328, 2006.

[Tkotz 1995] Tkotz, R., Gortler, A., Christiansen, J., Dollinger, S., Frank, K., Heine, F., Herleb, U., Insam, S., Kowalewicz, R., Mehr, T., Polster, A., Prucker, U., Schlaug, M., and Schwandner, A., “Pseudospark S witches-Technological Aspects and Applications,” IEEE Trans. Plasma Sci., vol. 23, no. 3, pp. 309-317, 1995.

[Vidal 1969] Vidal, C. R. and Cooper, J., "Heat-Pipe Oven: A New, Well-Defined Metal Vapor Device for Spectroscopic Measurements", Journal of Applied Physics 40, no.8, p. 3370, 1969.

[Wang 2005a] Wang, F., Kuthi, A., and Gundersen, M. A., “Compact high repetition rate pseudospark pulse generator,” IEEE Trans. Plasma Sci., vol. 33, no. 4, pp. 1177-1181, Aug. 2005.

[Wang 2005b] Wang, F., Liu, J. B., Sinibaldi, J., Brophy, C., Kuthi, A., Jiang, C., Ronney, P., and Gundersen, M. A., “Transient Plasma Ignition of Quiescent and Flowing Air/Fuel Mixtures,” IEEE Trans. on Plasma Sci., Vol. 33, No. 2, pp. 844-849, April 2005.

[Wang 2002] Wang, T., Liu, Y. H., Lee, Y. B., Ao, J. P., Bai, J. and Sakai, S., “1 mW AlInGaN-based ultraviolet light-emitting diode with an emission wavelength of 348 nm grown on sapphire substrate”, Appl. Phys. Lett., vol. 81, pp. 2508-1510, 2002.

[Wilson 2004] Wilson, I., “The compact linear collider CLIC”, Phys. Rep., vol. 403-404, pp. 365-378, 2004.